First posted online on 9 February 2021 as 10.1242/dmm.048116
Access the most recent version at http://dmm.biologists.org/lookup/doi/10.1242/dmm.048116

Multiscale molecular profiling of pathological bone resolves sexually dimorphic control of extracellular matrix composition.

Authors and affiliations

Aikta Sharma[a*], Alice Goring[a], Peter B. Johnson[b], Roger J.H. Emery[c], Eric Hesse[d], Alan Boyde[e], Bjorn R. Olsen[f], Andrew A. Pitsillides[g], Richard O.C. Oreffo[h], Sumeet Mahajan[b*] and Claire E Clarkin[a].

[a] School of Biological Sciences, Highfield Campus, University of Southampton, SO17 1BJ, United Kingdom of Great Britain and Northern Ireland.

[b] School of Chemistry and Institute for Life Sciences, Highfield Campus, University of Southampton, SO17 1BJ, United Kingdom of Great Britain and Northern Ireland.

[c] Department of Surgery and Cancer, Faculty of Medicine, St Mary's Campus, Imperial College London, London, W2 1PG, United Kingdom of Great Britain and Northern Ireland.

[d] Institute of Molecular Musculoskeletal Research, Faculty of Medicine, LMU Munich, Planegg-Martinsried, Germany.

[e] Dental Physical Sciences, Barts and The London School of Medicine and Dentistry, Queen Mary University of London, London, E1 4NS, United Kingdom of Great Britain and Northern Ireland.

[f] Department of Developmental Biology, Harvard School of Dental Medicine, Boston, Massachusetts, United States of America.

[g] Department of Comparative Biomedical Sciences, Royal Veterinary College, London, NW1 0TU, United Kingdom of Great Britain and Northern Ireland.

[h] Centre for Human Development, Stem Cell and Regeneration, Institute of Developmental Sciences, Faculty of Medicine, University of Southampton, SO16 6YD, United Kingdom of Great Britain and Northern Ireland.

*** Corresponding author(s)**

Aikta Sharma, School of Biological Sciences, Highfield Campus, University of Southampton, SO17 1BJ, as35g13@soton.ac.uk. Orcid ID: 0000-0002-5449-358X; Sumeet Mahajan, School of Chemistry and Institute for Life Sciences, Highfield Campus, SO17 1BJ, (023) 8059 2591, S.Mahajan@soton.ac.uk. Orcid ID: 0000-0001-8923-6666.

Keywords

Polarisation-resolved second harmonic generation, Raman spectroscopy, sexual dimorphism, extracellular matrix, collagen, VEGF.

Abbreviations

BMD, bone mineral density; BSE-SEM, backscattered electron scanning electron microscopy; CT-FIRE, curvelet transform-fibre extraction; ECM, extracellular matrix; HA, hydroxyapatite; OB, osteoblast; OBVEGFKO, osteoblast-specific *Vegf* deletion; OcnVEGFKO, osteocalcin-specific conditional *Vegf* deletion; OI, Osteogenesis Imperfecta; PMMA, poly-methyl methacrylate; p-SHG, polarisation-resolved second harmonic generation; ROI, region of interest; TFJ, tibiofibular junction; TPEF, two-photon excitation fluorescence; VEGF, vascular endothelial growth factor.

Summary statement

The combined application of polarisation-resolved Second Harmonic Generation microscopy with Raman spectroscopy has identified unique, sexually dimorphic extracellular matrix signatures linking pathological matrix disorganisation with composition.

Abstract

Collagen assembly during development is essential for successful matrix mineralisation, which determines bone quality and mechanocompetence. However, the biochemical and structural perturbations that drive pathological skeletal collagen configuration remain unclear. Deletion of vascular endothelial growth factor (VEGF) in bone forming osteoblasts (OBs) induces sex-specific alterations in extracellular matrix (ECM) conformation and mineralisation coupled to vascular changes, which are augmented in males. Whether this phenotypic dimorphism arises as a result of the divergent control of ECM composition and its subsequent arrangement is unknown and is the focus of this study. Herein, we have used a murine osteocalcin-specific *Vegf* knockout (OcnVEGFKO) and performed *ex vivo* multiscale analysis at the tibiofibular junction of both sexes. Furthermore, we also deleted *Vegf in vitro* in OBs extracted from male and female mice in an attempt to link sex-specific matrix signatures to deviations in gene expression. Label-free and non-destructive polarisation-resolved second harmonic generation microscopy (p-SHG) revealed a reduction in collagen fibre number in males following the loss of VEGF, complemented by observable defects in matrix organisation by backscattered electron scanning electron microscopy. This was accompanied only in males by localised divergence in collagen orientation, determined by p-SHG anisotropy measurements, as a result of OcnVEGFKO. Raman spectroscopy confirmed the effect on collagen was linked to molecular dimorphic VEGF effects on collagen-specific proline and hydroxyproline, and collagen intra-stand stability, in addition to matrix carbonation and mineralisation. V*egf* deletion in male and female murine OB cultures *in vitro* further highlighted divergence in genes regulating local ECM structure including *Adamts2*, *Spp1*, *Mmp9* and *Lama1*. The current results demonstrate the utility of macromolecular imaging and spectroscopic modalities for the detection of collagen arrangement and ECM composition in pathological bone. Linking the sex-specific genetic regulators to matrix signatures could be important for treatment of dimorphic bone disorders which clinically manifest in both pathological nano and macro-level disorganisation.

Introduction

Bone formation prevalent during development and repair is controlled by the co-ordinated expression of genetic regulators of osteoblast (OB) behaviour and commitment, and is characterised by the formation of non-mineralised osteoid comprising predominantly type I collagen (Reviewed in Blair et al. (2016)). The three-dimensional configuration of the osteoid scaffold, organised in part by the OB-derived non-collagenous proteins, subsequently facilitates the nucleation of apatite crystals during the mineralisation process (Blair et al., 2016; Houston et al., 2004; Staines et al., 2012). Both collagen organisation and the extent of matrix mineralisation influence the mechanosensitivity of bone. The hydroxyapatite (HA) crystals, deposited during matrix mineralisation, can withstand up to four times the stress of the collagen fibrils whereas the bulk collagen phase is responsible for providing flexibility and fracture resistance during the deformation response (Nair et al., 2013). This energy dissipation property of type I collagen in bone is largely due to its structure, in which fibrils made up of bundles of triple helical tropocollagen molecules containing a glycine-X-Y motif are organised into macroscale fibres (Currey, 1988; Donnelly et al., 2010; Ramshaw et al., 1998; Shoulders and Raines, 2009). A number of studies have shown that direct alterations to collagen properties implicate the overall mechanical properties of bone and often result in changes to fracture risk (Diebold et al., 1991; Kafantari et al., 2000; Sroga and Vashishth, 2012; Suarez et al., 1996).

The preclinical administration of collagen peptides have been shown to increase both the organic component of bone (Watanabe-Kamiyama et al., 2010) and enhance the biomechanical resistance of vertebrae in rats (de Almeida Jackix et al., 2010). Furthermore, clinical studies have demonstrated that specific collagen peptides can increase the bone mineral density (BMD) in postmenopausal women subjected to age-related bone loss (König et al., 2018). Conversely, during bone pathophysiology, the failure of appropriate osteoid mineralisation translates to an abnormal accumulation and distribution of the collagen matrix. This effect is prevalent in skeletal conditions such as osteomalacia or ‘soft bones’ wherein the proportion of mineral to collagen is reduced (Berry et al., 2002) whereas in osteogenesis imperfecta (OI) or ‘brittle bone disease’, the deficient bone matrix is hypermineralised in patients carrying mutations in the genes encoding the type I procollagen chains (*COL1A1* or *COL1A2*) (Boyde et al., 1999; Forlino et al., 2011).

The skeletal system is profoundly sexually dimorphic, being on average larger in men than women (Seeman, 2001). Bone strength is determined by bone mass acquisition during the pubertal years and subsequent bone turnover, which underlie sex differences in bone length, BMD, shape, and microarchitecture throughout life. Sex differences have been reported in diseases associated with mutations in collagen encoding genes. In an OI mouse model, Yao et al. reported sexual dimorphism linked to the structural and mechanical properties of bone (Yao et al., 2013), suggesting collagen-encoding genes exert a divergent influence upon male and female bones. Currently, little information exists on how collagen fibrils and mineral species interact at the molecular level, and how they influence the skeletal sexual dimorphism in bone development and disease. Identification of sex-specific

mechanisms of collagen assembly could provide novel targets to therapeutically improve bone structure, strength and reduce fracture risk in skeletal pathology.

Structurally type I collagen fibrils in bone, approximately 200 nm in length and 2–3 nm in diameter, undergo self-assembly resulting in the formation of larger supramolecular fibre structures with diameters of approximately 500 nm (Bai et al., 2013; Shoulders and Raines, 2009). The concentric and periodic stacking pattern of collagen molecules facilitates plate-shaped nanocrystal (10–20 nm in length and 2–3 nm in width) interactions, enabling further arrangement of the larger mineralised fibres into macro-level tissue structures. Polarisation-resolved second-harmonic generation (p-SHG) is a powerful non-destructive multiphoton modality that has been utilised previously for the study of collagen architecture and fibrillar orientation (Stoller et al., 2002). This technique has been used to inform and assess the pathological consequence of disease on the extracellular matrix (ECM) structure and conformation in a variety of cancers (Campbell et al., 2018; Chen et al., 2012; Tilbury et al., 2014b; Tokarz et al., 2019), fibrosis (James et al., 2019; Johnson et al., 2020; Lin et al., 2013; Rouède et al., 2017; Tilbury et al., 2014a) and in skin (Ducourthial et al., 2019; Fukushima et al., 2018; Su et al., 2009). Furthermore, p-SHG has been applied to investigate collagenous alterations that accompany ageing (Van Gulick et al., 2019), wound repair and scar formation (Mostaço-Guidolin et al., 2017). In a number of skeletal studies, SHG has also been used to; i) visualise woven bone formation during fracture repair (Park et al., 2019), ii) elucidate the effects of mechanical loading on collagen formation (Mansfield et al., 2019; Pinsard et al., 2019) and, iii) differentiate between normal and OI bone tissue (Nadiarnykh et al., 2007). To date however, multiscale quantitative analyses of collagen organisation, fibre alignment or anisotropy combined with the assessment of bone mineral composition within pathological bone have not been studied.

Vascularisation of the collagen matrix is a requirement for mineralisation and is driven, in part, by angiogenic factors produced by matrix-forming OBs, including vascular endothelial growth factor (VEGF) (Hu and Olsen, 2016; Liu et al., 2012). We recently reported that loss of *Vegf* in osteocalcin-expressing OBs (OcnVEGFKO) promotes a poorly mineralised, yet highly vascularised, bone patho-phenotype which is pronounced in males (Goring et al., 2019). *In vitro* studies confirmed this role of VEGF was in part mediated via autocrine signalling in male OBs, which resulted in compromised maturation. Murine long bones exist as compartmentalised structures with profound hierarchical arrangement observable on multiple levels. On the macroscale, trabecular and cortical structures (Fig. 1A and B) are visible and are distinct by their epiphyseal or diaphyseal localisation, respectively. Despite these differences in spatial organisation, nano-molecular type I collagen, and HA crystals, formed as a product of OB differentiation, constitute the majority of the mineralised ECM throughout the bone (Florencio-Silva et al., 2015) (Fig. 1C-E). In order to investigate the resultant effects of VEGF depletion at the macro and nanoscale, we combined p-SHG with Raman spectroscopy to characterise the spatial deviations in ECM organisation and composition. Linked with this multiscale analysis, we examined the potential mechanisms underlying the uncovered matrix signatures through the assessment of gene regulation *in vitro* following *Vegf* deletion in primary murine male and female OBs.

Results

Polarisation-resolved second harmonic generation imaging reveals alterations in collagen fibre number following VEGF deletion in males.

Dual-channel p-SHG and two-photon excitation fluorescence (TPEF) images could detect distribution of collagen fibres (p-SHG; blue), across the mineralised ECM (TPEF; green) at the tibiofibular junction (TFJ) of female wildtype (WT; Fig. 2A), female OcnVEGFKO (Fig. 2B), male WT (Fig. 2C) and male OcnVEGFKO (Fig. 2D) bone sections. Parallel backscattered electron scanning electron microscopy (BSE-SEM) images of these bones showed organised and mineral-embedded ECM displaying typical bone microstructure, comprised of vascular canals and osteocyte lacunae (Fig. 2E-G). In male OcnVEGFKOs, extensive collagen matrix disorganisation visible in pSHG/TPEF images (Fig. 2D) around blood vessel canals (Fig. 2Ii and Iii, BV; arrows) and osteocyte lacunae (Fig. 2Ii and Iii, triangles) appeared in the posterior cortex as patches of unmineralised osteoid in iodine-stained BSE-SEM images (Fig. 2H, Ji and Jii, Asterix). Moreover, additional patches of low p-SHG signal intensity were observed throughout the bone cortex (Fig. 2Iii, hatched area).

The cortical bone microstructure at the TFJ exhibits regional heterogeneity, with the highly vascularised posterior cortex exclusively exhibiting age-related changes in vascularity (Nunez et al., 2018). In line with this, we performed localised collagen fibre measurements posterior compartment following manual segmentation of the p-SHG TFJ images (Fig. 2K). Male animals were observed to have significantly greater number of collagen fibres than females in both WT and OcnVEGFKO animals (Fig. 2L and Fig. S1A-D). No significant differences in the number of fibres were observed following OcnVEGFKO in females however, fibre number/ μm^2 was significantly reduced in males compared to the respective WT controls. No significant interaction between sex and genotype on fibre number was reported following Two-Way Analysis of Variance (ANOVA).

Spatial anisotropy of fibrillar collagen following loss of VEGF in bone is sex-specific

Anisotropy determined from p-SHG images provided a quantitative measure of fibril alignment. This allowed us to assess the spatial organisation of the collagen fibrils within the ECM of OcnVEGFKO animals. To investigate whether the alterations to fibrillar alignment were responsible for the matrix-level abnormalities observed as a result of OcnVEGFKO, the mean anisotropy parameter, β, was calculated pixel-wise across the posterior region (Fig. 3A). The value of this parameter is variable between -0.5 and 1 (Campagnola et al., 2002), with these values signifying physical anisotropy or complete fibrillar alignment relative to the excitation laser polarisation with respect to their direction. In the opposing case, isotropic or random fibrillar alignment occurs exclusively when β=0. In the current study, values of β within the range of 0.5 to -0.5 were observed (Fig. 3A).

In the p-SHG anisotropy images, no significant differences in anisotropy, β, were observed across the total posterior region between the sexes and genotypes (Fig. 3A and D). BSE-SEM of iodine-stained sections of OcnVEGFKO bones highlighted distinctive and compartmentalised alterations in the ECM organisation particularly in males (Fig 3B and C; right). We subsequently undertook further analysis within this region of interest (ROI) including the endosteal and periosteal areas (Fig. 3A; middle) and around the vascular canals (Fig. 3A; right). Sex differences in fibril alignment were only apparent in WT animals in the endosteal regions, with fibrils being significantly more anisotropic in females versus males (1.81-fold, Fig. 3E). In addition, within this region, loss of VEGF in female OcnVEGFKO animals resulted in a reduction in anisotropy (-4.19-fold) versus WT alone (Fig. 3B and E), which was not evident in either the periosteal or perivascular regions (Fig. 3B, F and G). In contrast, in the periosteal and perivascular regions, OcnVEGFKO significantly decreased anisotropy in males by 1.97 and 2.64-fold, respectively (Fig. 3C, F and G), which may be contributing to the observable divergence in matrix organisation between the sexes throughout the posterior cortex. To assess the interaction between sex and genotype on anisotropy for each ROI, Two-Way ANOVA was conducted. A significant interaction between sex and genotype was exclusively reported in the endosteal regions (Fig. 3E), with no additional interactions detected for the total posterior, periosteal or perivascular regions (Fig. 3D, F and G respectively).

Sexual dimorphism in molecular extracellular matrix signatures following loss of VEGF identified by Raman spectroscopy

Raman spectroscopy was conducted to assess if the visible defects in the organisation of the bone matrix collagen, in the posterior cortex, was driven in part by alterations in composition following VEGF loss. Spectral deviations in collagen-specific species including proline (853 cm^{-1}) and hydroxyproline (876 cm^{-1}), HA mineralisation ($v_1PO_4^{3-}$; 960 cm^{-1}) and HA crystallinity (full-width half maximum; FWHM at 960 cm^{-1}), B-type carbonate (1070 cm^{-1}) in addition to noted fluctuations in amide III (1242 cm^{-1}) and amide I (1660 cm^{-1}) were detectable across animals (Fig. 4A). To quantify the basal sex differences in WT and OcnVEGFKO animals, in addition to the effect of VEGF loss in OcnVEGFKO animals on type I collagen, the 852 cm^{-1} and 876 cm^{-1} bands for proline and hydroxyproline respectively were selected due to their respective frequency in the glycine-X-Y repeat of type I collagen (Shoulders and Raines, 2009). Proline levels were 1.17-fold higher in female WTs versus males exclusively (Fig. 4B). Additionally, OcnVEGFKO had no effect on proline levels in females however, a significant elevation was observed in OcnVEGFKO males (+1.29-fold) compared to WT controls. Sex was also observed to influence hydroxyproline, with the levels in both female WT and OcnVEGFKO posterior cortices being 1.19-fold and 2.30-fold higher than in the male WT and OcnVEGFKOs, respectively (Fig. 4C). A small but significant reduction in hydroxyproline levels were induced following VEGF loss in females (-1.25-fold) with considerably larger reductions (-2.43-fold) detected in OcnVEGFKO males. The imbalance in the levels of these collagen-specific components can lead to modifications in the stability of the intra-strand links in type I collagen molecules. Calculated by the area ratio of the hydroxyproline to proline

bands in Raman spectra, the only detectable sex difference in collagen intra-strand stability were between OcnVEGFKO animals with stability being 2.97-fold higher in females versus males (Fig. 4D). The intra-strand stability was not affected by OcnVEGFKO in females however a 3.06-fold reduction was noted in male OcnVEGFKO animals versus the respective WTs.

Upon the inspection of mineral components, including HA and carbonate species, further sex differences were apparent. The levels of HA detected in the posterior cortex were greater in female WTs (+1.14-fold, Fig. 4E) and more crystalline (+1.04-fold, Fig. 4F) than that in males. While no differences in HA levels between OcnVEGFKO animals were detected, VEGF loss translated in the reduction of HA and loss in crystallinity in females (-1.27-fold, Fig. 4E and -1.02-fold, Fig. 4F respectively) versus controls. In contrast, OcnVEGFKO in males resulted in a 1.07-fold reduction in HA and a 1.12-fold reduction in crystallinity (Fig. 4E and F) versus WT. Throughout the dynamic process of apatite maturation, phosphate ions within the mineral lattice are susceptible to ionic substitution, with the most common being that for carbonate ions. Therefore, we examined the effect of sex and the consequential effect of the VEGF depletion on the presence of such carbonate species within the ECM. In WTs and in OcnVEGFKO animals, sex was observed to affect the levels of B-type carbonate divergently. In WTs, carbonate levels were 1.28-fold higher in the females than males, whereas in OcnVEGFKO animals, the levels of carbonate were 2.64-fold higher in the males versus females (Fig. 4G). Similar divergence in carbonate species levels were evident following OcnVEGFKO. In females, OcnVEGFKO resulted in a significant, 2.79-fold reduction in B-type carbonate levels, while in contrast a 1.21-fold increase in carbonate presence was detected in male OcnVEGFKO animals.

These oppositional changes in the bone ECM composition, were further reinforced by the mineral/matrix ratio, the carbonate/matrix ratio and the carbonate/phosphate ratio, which are typically used to report bone quality and predict changes in mechanical competence (Mandair and Morris, 2015). Sex in WT animals had no effect on the mineral/matrix ratio, commonly used to define matrix maturity, whereas a 1.21-fold reduction was observed in male versus female OcnVEGFKOs. VEGF loss was also observed to implicate the matrix maturity, with 1.38-fold reductions evident in male OcnVEGFKO animals, with smaller reductions observed in female OcnVEGFKO animals compared to WT (-1.12-fold, Fig. 4H). Interestingly, the carbonate/matrix ratio, typically applied to estimate the extent of carbonate mineralisation and an indirect predictor of fracture risk, was similarly affected by sex. Like with the mineral/matrix ratio, sex had no effect in WT animals however the potential predisposition for fracture was greater in male versus female OcnVEGFKOs by 2.12-fold (Fig. 4I). Following OcnVEGFKO, the carbonate/matrix ratio in females was significantly reduced by 2.45-fold. In contrast, no significant differences in this ratio were detected in male OcnVEGFKO bone compared to WT controls. These changes were linked to the ionic substitution of carbonate for phosphate within the ECM as described by the carbonate/phosphate ratio. Mirroring the trends observed for the carbonate/matrix ratio, the carbonate/phosphate ratio was elevated by 2.53-fold in males OcnVEGFKOs versus females while no differences were detected between WT animals. VEGF loss was observed to significantly reduce this ratio by 2.4-fold in OcnVEGFKO females but increased by 1.18-fold in OcnVEGFKO males compared to WT (Fig. 4J). Two-Way ANOVA reported a significant interaction between sex and genotype for all

Raman bands and ratios, with the exception of HA crystallinity in which no interaction between sex and genotype was detected (Fig. 4B-J).

Regulation of extracellular matrix genes in male and female osteoblasts following *Vegf* deletion

To elucidate the potential transcriptional regulators underlying the sexual dimorphism of the ECM, *Vegf* expression was deleted in OBs extracted from male and female mice (denoted OBVEGFKO, Fig. 5A) *in vitro* prior to gene expression analyses using an ECM quantitative PCR (qPCR) array. Successful loss of VEGF protein release was confirmed by VEGF-A ELISA of culture media, in both male (98.6%) and female (96.1%) *Vegf*-deficient OBVEGFKO cells versus WT cells (Fig. 5B).

Male WT OBs expressed lower levels of mRNA transcripts for genes associated with ECM formation and mineralisation versus female WT, including type I collagen (*Col1a1*;-1.14-fold), the ECM binding integrin α2 and αE subunits (*Itga2* and *Itgae*; -1.21 and -1.1-fold respectively) and secreted phosphoprotein 1/osteopontin (*Spp1;* -1.11-fold; Fig. 5C and G). Such trends were not apparent between OBVEGFKO cultures, as the expression of *Col1a1*, *Itga2* and *Spp1* were upregulated by 1.48, 2.62 and 1.15-fold respectively in male versus female OBVEGFKO cells with the exception of *Itgae* which was downregulated by 8.86-fold in male versus female OBVEGFKOs (Fig. 5D and F). Following *Vegf* deletion in female OBs, these mRNA transcript levels were upregulated versus WT (*Col1a1*; +3.17-fold, *Itga2*; +1.56-fold and *Spp1*; +2.99-fold, Fig. 5E and G). These transcriptional changes induced by the OBVEGFKO were further enhanced in male cells, with larger fold changes in mRNA expression observed versus WT controls (*Col1a1*; +5.33-fold, *Itga2*; +4.92-fold and *Spp1*; +3.59-fold; Fig. 5F and G). Interestingly *Itgae* expression appeared to be dimorphically regulated by *Vegf* as transcript levels were upregulated by 3.28-fold in female OBVEGFKOs but downregulated by 2.48-fold in male OBVEGFKOs versus their respective WT (Fig. 5G).

Interrogation of the genes involved in matrix remodelling revealed that the male WT OBs also expressed lower basal levels of A disintegrin-like and metallopeptidase with thrombospondin type 1 motif 2 (*Adamts2*; -1.31-fold), hemolytic complement (*Hc*; -1.44-fold) and secreted acidic cysteine rich glycoprotein/osteonectin (*Sparc*; -1.33-fold) than females whereas matrix metallopeptidase 13 (*Mmp13*) mRNA levels were 1.83-fold higher in the male versus female WT cells. Contrasting with this, OBVEGFKO was observed to induce differential effects on the expression of these genes with male *Vegf*-deficient OBs expressing higher levels of *Adamts2* (+1.63-fold), *Mmp13* (+1.19-fold) and *Sparc* (+1.54-fold) versus female OBVEGFKO cells. Similarly to *Itgae*, *Hc* mRNA expression was also downregulated by 8.72-fold in male versus female OBVEGFKOs. Following the loss of *Vegf*, *Hc* expression levels were dimorphically influenced by OBVEGFKO; upregulated by 3.18-fold in female OBVEGFKOs versus WT but downregulated by 1.9-fold in male OBVEGFKOs versus WT. *Adamts2* (+1.6 and +3.44-fold respectively), *Mmp13* (+5.51 and +3.59-fold respectively) and *Sparc* (+1.74 and +3.57-fold) expression levels were upregulated in both OBVEGFKO female and OBVEGFKO male cultures respectively compared to WT controls.

Given OB-derived VEGF is an important regulator of angiogenesis, mediated via paracrine signalling to endothelial cells, we additionally investigated the effect of sex in *Vegf*-expressing and deficient cells, in addition to the effect of *Vegf* depletion in male and female OBVEGFKO cultures on the expression of genes associated with autocrine control of pro-angiogenic bone matrix formation. The expression of genes encoding; laminin subunit α1 (*Lama1*), matrix metallopeptidase 9 (*Mmp9*) and thrombospondin 1 (*Thbs1*) were lower in male versus female WTs (-1.48, -1.07 and -1.19-fold respectively) but higher in male versus female OBVEGFKO cells (+2.76, +1.24 and +1.2-fold respectively). Interestingly, OBVEGFKO resulted in the upregulation of *Lama1* (+1.96-fold), *Mmp9* (+3.37-fold) and *Thbs1* (+3.09-fold) in females versus WT. To a similar extent, *Vegf* loss translated in extensive upregulation of these genes in male OBVEGFKO cells (+7.89, +4.44, and +4.39-fold respectively) in comparison to the WT controls, with higher overall expression changes observed following OBVEGFKO in males than females (Fig. 5E-G).

Discussion

The combination of multimodal p-SHG and TPEF imaging with Raman spectroscopy has revealed that the compositional abnormalities in pathological bone are associated with structural alterations in collagen conformation and matrix mineralisation. Uniquely, these techniques have enabled the thorough assessment of the nanoscale sex differences combined with the consequential effects of the loss of VEGF. Previous studies linked the loss of VEGF to bone pathology characterised by a profound osteoporotic phenotype present following the deletion of *Vegf* in early and late-stage OBs (Goring et al., 2019; Liu et al., 2012). Furthermore, clinical reports have also identified that the loss of VEGF is associated with degenerative bone loss seen in osteoporosis (Senel et al., 2013).

Label-free p-SHG imaging of calcified tibial sections from OcnVEGFKO animals identified a reduction in the number of collagen fibres exclusively in the male bones, which were localised to the highly vascularised posterior region of the TFJ. Anisotropy in p-SHG signals revealed variations in fibrillar collagen organisation and highlighted distinctive, sex-specific alterations in the endosteal compartment of the posterior cortex in female OcnVEGFKOs and in periosteal and perivascular regions in male OcnVEGFKOs. Raman spectroscopy further identified that these localised deviations in the arrangement of the collagenous matrix following VEGF loss were associated with divergence in the levels of nano-molecular ECM components. Specifically, in the male OcnVEGFKO bone alone, deviation in the ratio of hydroxyproline to proline indicated further dimorphism in fibrillary collagen conformation and integrity at the nanoscale level. While the collagen content of bone is an important determinant of toughness and resistance to fracture (Boskey et al., 1999; Nyman and Makowski, 2012; Unal et al., 2018), the strength of bone is largely dictated by its mineral phase (Burstein et al., 1975; Morris and Mandair, 2011; Viguet-Carrin et al., 2006). In both male and female bone, the loss of VEGF in OcnVEGFKO animals resulted in reductions in the levels of HA. These trends were extended to the mineral/matrix ratio, used to assess the extent of matrix mineralisation in bone (McCreadie et al., 2006). These dimorphic matrix signatures were linked to a number of genes involved in matrix arrangement

which exhibited divergent regulation following the deletion of *Vegf* in male and female OBs *in vitro*. As the sexual dimorphism observed in fibrillary collagen arrangement and ECM composition were apparent at the nanoscale level, we report novel findings and demonstrate the robust analytical capabilities of complementary techniques that can link the molecular manifestations to the sex-specific deficiencies in matrix organisation observed at the macroscale level.

The material properties of bone are determined by both the mineral and organic constituents of the ECM. Thus, bone strength and flexibility, independent of bone mass, are ultimately compromised by deficiencies in composition. Previous investigations have reported that the collagen fibrils in cortical bone adopt a preferential alignment with anisotropic fibrils bearing alignment transverse to the long axis, enabling resistance to compressive forces whereas those orientated longitudinally confer enhanced resistance to tensile forces (Ascenzi and Benvenuti, 1986; Augat and Schorlemmer, 2006; Li et al., 2013; Martin and Boardman, 1993; Morgan et al., 2018; Simkin and Robin, 1974). We predict the reductions in the number of collagen fibres and localised anisotropy around the periosteal and perivascular regions of the posterior cortex in male OcnVEGFKO bone may contribute to a sex-specific divergence in mechanical properties. This idea is supported by BSE-SEM imaging of the male OcnVEGFKO TFJ cortex, which highlighted extensive areas of unmineralised osteoid were densely confined around the vascular canals that coalesced with areas of diffuse p-SHG signal. A principal idea surrounding anisotropy in bone, is that orientation of collagen fibres and nucleating mineral crystals bears alignment to the direction of bone growth (Wang et al., 2012). Therefore, zonal alterations to fibril anisotropy observed in the OcnVEGFKO bone may reveal developmental adaptation confined to specific areas, such as abnormal vascular canal growth within the bone cortex. As a consequence, this may primarily result in irregularities in collagen organisation that lead to further secondary deficiencies in matrix mineralisation.

Aside from structural organisation, the chemical composition of bone is an important contributor of bone quality and strength (Mandair and Morris, 2015; Morris and Mandair, 2011). As the deposited collagen functions as a scaffold for bone mineralisation, we investigated if dimorphic changes in the levels of collagen-specific species following OcnVEGFKO are related to the defective mineralisation phenotype. Type I collagen molecules are structurally composed of a triple amino acid repeat (Gly-X-Y), with the most abundant amino acids in the X and Y position being proline (28%) and hydroxyproline (35%) representing the most common triplicate motif (Ramshaw et al., 1998). Using Raman spectroscopy, we showed that elevations in proline and reductions in hydroxyproline were present in OcnVEGFKO males whereas only hydroxyproline levels were reduced in females following VEGF loss. The transition from proline to hydroxyproline in collagen molecules occurs as a post-translational event and is critical for the folding of the collagen triple helix into fibrillary structures, enhancing internal hydrogen bonding between adjacent polypeptide chains (Bansal et al., 1975). As a result, the imbalances in hydroxyproline to proline levels assessed in the collagen intra-strand stability ratio (Olejnik et al., 2016; Sharma et al., 2020) indicated severe compromise in the conformational stability of the collagen fibrils only occurs in the male OcnVEGFKOs. We also noted reductions in the levels of HA and mineral crystallinity in both male and female OcnVEGFKO bones, alongside sexually dimorphic deviations in carbonate levels. HA

crystals in bone exist as nanocomposite platelet structures that can readily accommodate ionic substitution of anionic phosphate at the PO_4^{3-} sites (B-site), with the most commonly replacement being that with carbonate (B-type (Madupalli et al., 2017; Morris and Mandair, 2011)). The effect of carbonate substitution within the apatite lattice is relatively well documented, with studies using vibrational spectroscopies and X-ray diffraction reporting inverse relationships of carbonate content in bone with mineral crystallinity (McElderry et al., 2013; Pleshko et al., 1991). In line with our findings, reductions in B-type carbonate levels in the female OcnVEGFKO cortex coincided with relatively small reductions in the HA crystallinity. In comparison in males, carbonate levels were significantly increased and greater reductions in crystallinity were observed following OcnVEGFKO, strongly indicating that biomechanical deficit and fracture susceptibility may occur in a sex-specific manner as a consequence of the VEGF loss (Mandair and Morris, 2015; Morris and Mandair, 2011; Yerramshetty and Akkus, 2008).

Bone strength, determined by the acquisition of peak bone mass, is regulated during puberty and determines the sex differences in bone length, BMD, geometry, and microarchitecture that persist into adulthood and old age. The sexually dimorphic control of the material properties of bone however continue to be poorly understood, and whether diversity in genetic regulators of collagen formation and arrangement translate in regionalised differences in cortical bone pre-pubertally remains an intriguing possibility. Supporting our findings in mice, age-related and regional gender-differences in collagen fibre orientation have been reported in humans (Goldman et al., 2003). Furthermore, sexual dimorphism in collagen production was recently reported in the skin of mice, as a result of divergence in the expression of type I collagen mRNA during postnatal skin development at the onset of puberty (Arai et al., 2017). In bone, mutations in genes encoding type I collagen result in OI, a developmental pathology characterised by a distinctive and extremely fragile skeletal phenotype (Bai et al., 2013; Chen et al., 2012; Stoller et al., 2002; Yao et al., 2013). Previous multiscale analyses of a murine OI model utilised a combination of micro-computed tomography and three-point mechanical bending with Raman spectroscopy revealed sex-specific trends in geometrical, mechanical, and compositional parameters (Yao et al., 2013). Sexual dimorphism was reported in cortical and trabecular bone morphology with male OI mice having greater bone mass and as a result, increased biomechanical strength. However, associated differences were not evident in hydroxyproline content, in the mineral/matrix, the carbonate/matrix or the carbonate/phosphate ratio between male and female OI animals. This result was somewhat surprising as the authors concluded that mineral and matrix components in OI bone do not exhibit the same gender dependency as the induced geometrical and biomechanical deficits in the tibial cortex of their murine model. An alternative explanation, and possible limitation, is that the Raman spectra were averaged across the anterior, lateral, medial and posterior compartments, causing potential dilution of any detectable regionalised effects.

The involvement of sex hormones in controlling the sex-specific deviations in matrix composition is an interesting question. Although the role of oestrogen in regulating collagen production in skin is well investigated (Arai et al., 2017; Brincat et al., 1987; Markova et al., 2004; Son et al., 2005), controversy surrounding the response of osteoblastic cells to sex steroids during bone collagen synthesis remains (Canalis and Raisz, 1978; Keeting et al., 1991; Majeska et al., 1994; Wiren et al., 2008). In the present

study, successful *in vitro* culture of male and female OBs was achieved in the absence of circulating hormones. In addition, the expression of both oestrogen and androgen receptors in OBs derived from male and female mice were comparable (Goring et al., 2019). Deletion of *Vegf* in male and female OBs influenced the expression of genes associated with ECM formation and arrangement, confirming a potential intracrine and/or autocrine role of VEGF signalling in bone. Consistent with a reduction in mineralisation in the male OcnVEGFKOs, we report elevated expression of genes associated with matrix remodelling and angiogenesis in male *Vegf* deficient OBs. Furthermore, upregulation of a range of genes linked to collagen biosynthesis including *Adamts2* and the type I collagen-specific integrin complex encoded by *Itga2* (integrin alpha-2 subunit; α2) and *Itgb1* (integrin beta-1 subunit; β1, data not shown) with expression levels consistently higher in the male OBVEGFKOs than female cells. ADAMTS2, is highly expressed in a range of tissues rich in type I collagen, including bone, and is involved in the cleavage of the N-terminal sequence from the pro-peptide. Removal of the pro-peptide sequences are essential for the generation of functional collagen monomers that are capable of extracellular fibril assembly, with inherited deficiencies in this protein resulting in skin fragility in patients with dermatosparactic Ehlers-Danlos syndrome (Bekhouche and Colige, 2015; Le Goff et al., 2006). Conversely, the upregulated expression of *ADAMTS2* has been documented in the genomic assessment of fibrous dysplasia (Zhou et al., 2014), which is characterised overproduction of the ECM specifically in bone. Intriguingly, the skeletal phenotype observed in the male OcnVEGFKO bones display a number of parallels to those seen in fibrous dysplasia patients, particularly the increased prevalence of woven bone (Burke et al., 2017) containing randomly orientated collagen fibrils are in line with our own findings. Complementing this, we also detected a drastic upregulation in the expression of the α2β1 integrin mRNA expression in male *Vegf* deficient cells in comparison to females. Previously, the elevated expression of the integrin α2 subunit has been shown to positively regulate the expression of the *Col1a1* gene, leading to the synthesis of type I collagen (Riikonen et al., 1995). We speculate that the combined effects of upregulated *Itga2* expression with *Adamts2* in the male OBVEGFKO cells, may in fact be contributing significantly to the excessive and disorganised sex-specific matrix phenotype observed in the OcnVEGFKO bone cortex.

We also noted further sex-specific variations in the mRNA levels of genes associated with angiogenesis. Laminin-1, recognised by α2β1 integrins, exhibits pro-angiogenic effects in the vascular endothelium. Both *Lama1* and *Mmp9* expression exhibited greater upregulation in male OBVEGFKO cells than females. In particular, elevated levels of MMP9 correlate with osteoporotic bone loss (Haibo et al., 1997), and given its function in matrix remodelling, these findings indicate possible pathological remodelling effects that could in part be responsible for the aberrations in matrix microarchitecture and vascular anomalies in the male OcnVEGFKO bones (Goring et al., 2019). Contrasting with these effects, differential changes in the expression of hemolytic complement and integrin alpha E subunit/CD103 were detected following OBVEGFKO in males and female OBs. Reductions in hemolytic complement, in contrast to MMP9, are associated with the pathogenesis of degenerative bone loss (Ehrnthaller et al., 2013). Deficiencies in *Hc* have also been shown to severely reduce the mechanical competence of bone following fracture due to impaired fracture healing (Ehrnthaller et al., 2013). In the

current study, we noted sexual dimorphism in the expression of *Hc* following OBVEGFKO *in vitro* with upregulation of mRNA transcripts detected in female OBs and downregulated expression in male OBs, indicating that additional and alternative mechanisms involving the immune system may also contribute to the alterations to the ECM.

In summary, the present study has demonstrated the combined application of p-SHG with Raman spectroscopy can provide a quantitative, non-destructive approach to characterise the arrangement and composition of the bone matrix on multiple hierarchical levels (Fig. 6). In the context of VEGF we have found that its deletion in osteocalcin-expressing cells dramatically affects the bone matrix; hallmarked by pronounced alterations to collagen matrix organisation, localised alterations in fibrillar anisotropy and mineralisation. Alterations in genes linked to ECM also appear to be sex-specific in OBs. Enhanced understanding of the sex-specific genetic control of the arrangement of the bone matrix could therefore be used to therapeutically modulate dysfunctional mineralisation at the onset of bone pathology or promote fracture repair processes distinctively in males and females.

Materials and Methods

Specimen preparation

Tibiae from 16-week male and female *Vegf*$^{fl/fl}$ (WT) and *Vegf*$^{fl/fl}$*;Ocn-Cre* (OcnVEGFKO) littermates were derived as previously described (Goring et al., 2019) in accordance with the UK Animals (Scientific Procedures) Act 1986 and regulations set by the UK Home Office. Briefly, tibiae were fixed for 48 hours on rotation in 4% formaldehyde, pH 7.4 (from paraformaldehyde; Merck, UK) and dehydrated in ethanol ahead of embedding in poly-methyl methacrylate (PMMA). 5 µm thick cross sections were cut in the region of the tibial diaphysis termed the TFJ (Fig. 1A and B respectively). This region was selected given the clear and distinctive morphology of the TFJ as a landmark area for uniform interrogation of the ECM and its components (Fig. 1C-E) across the genotypes and sexes (Goring et al., 2019; Javaheri et al., 2015; Nunez et al., 2018). Data presented are representative of sections from three littermate matched WT and OcnVEGFKO animal pairs.

Second Harmonic Generation microscopy

SHG images were acquired using a home-built multiphoton laser scanning system consisting of; a tuneable, pulsed femtosecond laser (Titanium:Sapphire laser; Mai Tai®, Spectra-Physics, USA; 710 – 990 nm, 100 fs, 80 MHz) coupled to an upright Leica DMRB microscope through a pair of galvanometric mirrors for laser scanning (Fig. 7). The fundamental laser beam, tuned at 808 nm for p-SHG microscopy, first passes through a beam expander before being directed towards and focused onto the sample by a microscope objective. The resulting signal is backwards collected by the objective and directed to a dichroic beam splitter (cut-off at 685 nm; FF685-DI02-25X36, Semrock, USA) followed by a short pass-filter (cut-off at 694 nm) allowing for separation of signal from the excitation beam. A second long pass

dichroic beam splitter (cut-off at 458 nm; FF458-DI02, Semrock, USA) in the detection path enables separation of SHG from TPEF before passing through narrow band-pass filters (400 ± 20 nm for SHG; FB400-40, Thorlabs, and 520 ± 20 nm for TPEF; FBH520-40, Thorlabs, USA) to facilitate the transmission of selected wavelengths prior to their detection by separate photomultiplier tubes (PMTs; H10722-01 and H10722-20 respectively, Hamamatsu, Japan). For circular p-SHG imaging, the polarisation of the fundamental in the excitation path was controlled using a quarter waveplate (λ/4; zero-order, 808 nm, Thorlabs, USA). A half waveplate (λ/2; WPH10M-808, Thorlabs, USA) was further used to correct for ellipticity in the system (generated by non-45° reflections within the scanning system) enabling circular polarisation at the focus. For the determination of anisotropy, p-SHG images were acquired at orthogonal polarisations (parallel and perpendicular to the laser polarisation) using a linear polarisation analyser (LPVISE100-A; 400-700nm, Thorlabs, USA) which was placed ahead of the PMT in the SHG detection path exclusively. All p-SHG images of bone sections were acquired using either an 20x air objective with an numerical aperture (NA) of 0.7 (Leica, Germany; Fig. 2 and 3) or 63x water immersion objective with NA of 1.2 (Leica, Germany; Fig. S1) in tandem with the MATLAB ScanImage interface (Vidrio Technologies, USA, (Pologruto et al., 2003)), providing a field of view of approximately 313 µm x 313 µm or 249 µm x 249 µm respectively. Laser power at the specimen was approximately 30 mW. Image acquisition settings included 3x optical zoom with three acquisitions collected over a period of 8 to 16 milliseconds per line for a 512 x 512-pixel image. Images were processed using FIJI (Schindelin et al., 2012). Exemplary p-SHG images obtained by circularly and linearly polarised excitation beam are shown in Fig. S2. Due to the limited lateral field of view, tiled images were taken in 200 µm steps in the x- and y- planes across the TFJ section, intensity normalised in FIJI then manually restitched using MosaicJ, a semi-automated ImageJ software plugin (Thevenaz and Unser, 2007) ahead of region-specific image analysis.

Collagen fibre analysis

For the quantitative assessment of collagen fibre number, curvelet transform-fibre extraction (CT-FIRE V2.0; https://loci.wisc.edu/software/ctfire, (Bredfeldt et al., 2014)) based analysis was performed on SHG images obtained exclusively using a circularly polarised input. Circular polarisation enables the equal excitation of all fibres independent of their orientation, in a given focal plane. Stitched p-SHG images of entire TFJ sections were segmented manually into the anterior, lateral, medial and posterior quadrants and saved as separate images using FIJI (Fig. 2K) in line with previous work (Nunez et al., 2018). All further regionalised analyses were performed on p-SHG images of the segmented posterior region. Prior to fibre analysis in CT-FIRE, all SHG images were converted to 8-bit format before batch processing using default settings recommended by the developers. Curvelet transform was performed first to denoise the image and enhance fibre edges followed by the application of the FIRE algorithm to extract the fibre number (Fig. 2K and L). Fibre number was normalised to the area of the segmented posterior quadrant, calculated using the freehand tool and measure function in FIJI.

Polarisation anisotropy calculation and analysis

For determining anisotropy in collagen fibril orientation, p-SHG images were obtained with the linear polarisation analyser orientated parallel (∥; 0 °) and orthogonal (⊥; 90 °) relative to the excitation laser polarisation. The SHG anisotropy factor (β), varying from -0.5 to 1 (Chen et al., 2012) was calculated pixel-wise in stitched images of the posterior region of the TFJ using an in-house FIJI script satisfying the following equation: $I_{\parallel} - I_{\perp} / I_{\parallel} + 2I_{\perp} = \beta$, where $I_{\parallel}$ and $I_{\perp}$ indicate the recorded SHG intensity at polarisations parallel and perpendicular, respectively, to the excitation. For endosteal and periosteal anisotropy analysis, measurements were confined to one 120 µm x 25 µm sized ROI box placed on the respective areas per section. Similarly, for perivascular anisotropy analysis, measurements were restricted to five 100 µm x 100 µm sized ROI boxes placed over visible vascular canals.

Backscattered-electron-scanning electron microscopy

PMMA-embedded bone blocks were polished ahead of imaging with a Zeiss EVO MA10 SEM (Zeiss, Cambridge, UK) using an acceleration voltage of 20 kV and 49 Pa chamber pressure as previously described (Goring et al., 2019). Aqueous iodine in ammonium iodide or iodine vapour was used to stain the surface of PMMA blocks to enable the visualisation of cellular detail (Boyde et al., 2014; Boyde et al., 2017).

Raman spectroscopy

Raman spectra were acquired using the Renishaw InVia® Raman microscope (Renishaw plc, UK) equipped with a 532 nm continuous-wave solid-state laser with Gaussian beam profile, and 20x air objective with NA of 0.4 (Leica, Germany) yielding a diffraction limited spot size of approximately 815 nm. Incorporated in this system is a Rayleigh edge filter, 2400 lines/mm grating providing spectral resolution of approximately 1.06 cm^{-1} and Renishaw Peltier cooled charged coupled device detector. Intensity and wavenumber calibration of the instrument was achieved as previously described prior to spectral acquisition (Sharma et al., 2020; Smith et al., 2017). Spectra were collected within the "Fingerprint region" from 700 cm^{-1} to 1750 cm^{-1} (Vandenabeele, 2013) using single point static scans with an exposure time of 10 seconds, 100% laser power and three accumulations set using WiRE 3.4 (Renishaw plc, UK). Raman spectra, presented as class means, were obtained from 25 single and random points localised within the posterior cortex, identified as previously described (Nunez et al., 2018) from each bone section. Power at the specimen was approximately 37 mW.

Raman spectral processing and analysis

Cosmic ray artefacts acquired upon acquisition were removed as previously described (Sharma et al., 2020; Smith et al., 2017). IRootLab (Scott et al., 2013) was utilised for spectral pre-processing, ahead

of spectral deconvolution analysis, wherein class mean Raman spectra were denoised using Haar wavelets (6-point smoothing) and background corrected by the fitting of 7th order polynomial. Class mean spectra were intensity normalised to the Raman peak at 1450 cm^{-1} corresponding to the CH_2 wag vibration (Fig. 4A and S2A). Peak assignment of PMMA contributions in bone Raman spectra were identified following the inspection of unprocessed spectra obtained from visible areas of PMMA, devoid of bone, using the same experimental conditions (Fig. S2B). The 812 cm^{-1} peak was identified as a PMMA artefact and was not analysed further. We note that the 1450 cm^{-1} peak contains contributions of PMMA, thus in order to normalise for the varying amounts of PMMA detected in each successive point spectra, the 1450 cm^{-1} peak was selected for wavenumber and intensity normalisation, enabling consistency in spectral comparisons across the genotypes and sexes. Peak positions of Raman bands of interest corresponding to ECM and mineral components (proline; 853 cm^{-1}, hydroxyproline; 876 cm^{-1}, HA; 960 cm^{-1}, B-type carbonate; 1070 cm^{-1}; Fig. 4A and S3C) were identified from second-order derivative spectra (Fig. S3D) as previously described (Sharma et al., 2020). Peak area from class means spectra were extracted by spectral deconvolution whereby specified bands of interest were fitted with mixed Lorentzian and Gaussian curves using WiRE 4.1 (Renishaw plc, UK) as previously described in our aforementioned study.

Isolation and culture of osteoblasts

Primary long bone OBs from 4-day old male and female *Vegf*$^{fl/fl}$ mice were isolated using the collagenase-collagenase-EDTA-collagenase extraction method as previously described (Orriss et al., 2014). Prior to plating, cells were cultured in complete phenol-red free α-Minimum Essential Medium (41061, Gibco, UK) containing 10% heat inactivated fetal bovine serum (FBS; Gibco, UK), 50 µg/ml gentamicin (Merck, UK), 100 U/ml penicillin and 100 µg/ml streptomycin (Merck, UK) until 80% confluent in 75 cm^2 flasks (Thermofisher Scientific, UK). All cell cultures were maintained in a humidified incubator at 37°C and 5% CO_2 and used at passage 1.

Adenoviral transduction

Vegf expression was deleted in OBs, plated at a density of 250,000 cells per well, using adenovirus-Cre-GFP (denoted OBVEGFKO, 1045; Vector Biolabs, Philadelphia, USA) at a multiplicity of infection of 100 for six days. Viral transduction was performed in complete, phenol-red free α-Minimum Essential Medium as previously described (Goring et al., 2019). Adenovirus GFP (denoted WT, 1060; Vector Biolabs, Philadelphia, USA) was used as a control. Cells were stepped down in low serum media, containing 1% FBS for 24 hours, ahead of conditioned media collection for knockdown validation and RNA lysates collection for gene expression analysis. Fluorescence images of adenoviral transduced cells were acquired using the Deltavision Elite microscope using a 10x air objective with NA of 0.4 in combination with the SoftWoRx acquisition software (GE Healthcare Sciences, USA).

Validation of VEGF knockdown

A VEGF-A sandwich mouse ELISA kit and reagents (ab209882, Abcam, UK) was used to confirm VEGF knockdown in the collected conditioned media from male and female OBVEGFKO cells versus WTs following the manufacturer's instruction. Purified total RNA concentration was used to normalise VEGF-A concentrations quantified by the ELISA.

Quantitative PCR array

RNA were isolated and purified using the Monarch® Total RNA Miniprep kit (New England Biolabs, USA) according to the manufacturer's instructions. 500 ng RNA per preparation was reverse transcribed into cDNA using the GoScript Reverse Transcriptase kit (Promega, USA). Gene expression changes associated with ECM and adhesion molecules in male and female WT and OBVEGFKO samples were screened using an RT^2 Profiler™ PCR Array (PAMM-013Z, 330231; Qiagen, Germany) and the StepOnePlus Real-Time PCR system (Applied-Biosystems, UK) following the manufacturer's instructions. Ct values were normalised to housekeeping genes included in the array, and relative expression was calculated using the ΔΔCt method (Livak and Schmittgen, 2001).

Statistical Analysis

All investigators were blinded to the genotype and sex of animals throughout experimentation until data analysis. Data are expressed as the mean value ± standard error of the mean (SEM). Genotype effects between WT and OcnVEGFKO groups and sex effects between male and female groups were assessed using Student's t-test. Interaction between sex and genotype was determined using Two-Way ANOVA with Tukey's post-hoc test conducted for further comparisons. All statistical analysis was performed using GraphPad Prism 8 (GraphPad Software Inc, California, USA). $P<0.05$, denoted as *, was considered to be statistically significant. P values of <0.01, <0.001, and <0.0001 are denoted as **, *** and **** respectively.

Acknowledgements

The School of Biological Sciences, University of Southampton, UK, DOT Medical Implant Solutions, Germany, and Versus Arthritis, UK kindly funded this study.

Competing interests

No competing interests declared.

Funding

R.O.C.O. is supported by the UK Regenerative Medicine Platform, Acellular / Smart Materials – 3D Architecture (MR/R015651/1). S.M. acknowledges funding from European Research Council grant, NanochemBiovision (63258) and EPSRC grant EP/T020997/1.

Data availability

The complete quantitative PCR array dataset has been deposited in the Gene Expression Omnibus and are accessible through the Series accession number GSE164735 (https://www.ncbi.nlm.nih.gov/geo/query/acc.cgi?acc=GSE164735).

Author contributions

Conceptualization: A.S., A.B., A.A.P., R.O.C.O., S.M., C.E.C.; Methodology: A.S., P.B.J., E.H., A.B., B.R.O., A.A.P., R.O.C.O., S.M., C.E.C.; Software: A.S., P.B.J., S.M.; Validation: A.S., R.O.C.O., S.M., C.E.C.; Formal analysis: A.S., A.G., P.B.J.; Investigation: A.S., A.G., A.B.; Resource: A.G., E.H., A.B., B.R.O., S.M., C.E.C., Writing – original draft: A.S., R.O.C.O., C.E.C.; Writing – review & editing: A.S., A.B., B.R.O., A.A.P., R.O.C.O., S.M., C.E.C.; Visualization: A.S., R.O.C.O., S.M., C.E.C.; Supervision: R.O.C.O., S.M., C.E.C.; Project administration: A.S., C.E.C.; Funding acquisition: R.J.H.E., C.E.C.

References

Arai, K.Y., Hara, T., Nagatsuka, T., Kudo, C., Tsuchiya, S., Nomura, Y., Nishiyama, T., 2017. Postnatal changes and sexual dimorphism in collagen expression in mouse skin. PLoS One 12, e0177534-e0177534.

Ascenzi, A., Benvenuti, A., 1986. Orientation of collagen fibers at the boundary between two successive osteonic lamellae and its mechanical interpretation. J Biomech 19, 455-463.

Augat, P., Schorlemmer, S., 2006. The role of cortical bone and its microstructure in bone strength. Age and ageing 35 Suppl 2, ii27-ii31.

Bai, Y., Yin, G., Huang, Z., Liao, X., Chen, X., Yao, Y., Pu, X., 2013. Localized delivery of growth factors for angiogenesis and bone formation in tissue engineering. International Immunopharmacology 16, 214-223.

Bansal, M., Ramakrishnan, C., Ramachandran, G.N., 1975. Stabilization of the collagen structure by hydroxyproline residues. Proceedings of the Indian Academy of Sciences - Section A 82, 152-164.

Bekhouche, M., Colige, A., 2015. The procollagen N-proteinases ADAMTS2, 3 and 14 in pathophysiology. Matrix Biol 118.

Berry, J.L., Davies, M., Mee, A.P., 2002. Vitamin D metabolism, rickets, and osteomalacia. Semin Musculoskelet Radiol 6, 173-182.

Blair, H.C., Larrouture, Q.C., Li, Y., Lin, H., Beer-Stoltz, D., Liu, L., Tuan, R.S., Robinson, L.J., Schlesinger, P.H., Nelson, D.J., 2016. Osteoblast Differentiation and Bone Matrix Formation In Vivo and In Vitro. Tissue Engineering Part B: Reviews 23, 268-280.

Boskey, A.L., Wright, T.M., Blank, R.D., 1999. Collagen and Bone Strength. J. Bone Miner. Res. 14, 330-335.

Boyde, A., McCorkell, F.A., Taylor, G.K., Bomphrey, R.J., Doube, M., 2014. Iodine vapor staining for atomic number contrast in backscattered electron and X-ray imaging. Microscopy research and technique 77, 1044-1051.

Boyde, A., Staines, K.A., Javaheri, B., Millan, J.L., Pitsillides, A.A., Farquharson, C., 2017. A distinctive patchy osteomalacia characterises Phospho1-deficient mice. Journal of anatomy 231, 298-308.

Boyde, A., Travers, R., Glorieux, F.H., Jones, S.J., 1999. The Mineralization Density of Iliac Crest Bone from Children with Osteogenesis Imperfecta. Calcified Tissue International 64, 185-190.

Bredfeldt, J.S., Liu, Y., Pehlke, C.A., Conklin, M.W., Szulczewski, J.M., Inman, D.R., Keely, P.J., Nowak, R.D., Mackie, T.R., Eliceiri, K.W., 2014. Computational segmentation of collagen fibers from second-harmonic generation images of breast cancer. Journal of biomedical optics 19, 16007.

Brincat, M., Versi, E., Moniz, C.F., Magos, A., de Trafford, J., Studd, J.W., 1987. Skin collagen changes in postmenopausal women receiving different regimens of estrogen therapy. Obstet Gynecol 70, 123-127.

Burke, A.B., Collins, M.T., Boyce, A.M., 2017. Fibrous dysplasia of bone: craniofacial and dental implications. Oral Dis 23, 697-708.

Burstein, A.H., Zika, J.M., Heiple, K.G., Klein, L., 1975. Contribution of collagen and mineral to the elastic-plastic properties of bone. JBJS 57.

Campagnola, P.J., Millard, A.C., Terasaki, M., Hoppe, P.E., Malone, C.J., Mohler, W.A., 2002. Three-dimensional high-resolution second-harmonic generation imaging of endogenous structural proteins in biological tissues. Biophys J 82, 493-508.

Campbell, K., Chaudhary, R., Handel, J., Patankar, M., Campagnola, P., 2018. Polarization-resolved second harmonic generation imaging of human ovarian cancer. Journal of biomedical optics 23, 066501.

Canalis, E., Raisz, L.G., 1978. Effect of sex steroids on bone collagen synthesis in vitro. Calcif Tissue Res 25, 105-110.

Chen, X., Nadiarynkh, O., Plotnikov, S., Campagnola, P.J., 2012. Second harmonic generation microscopy for quantitative analysis of collagen fibrillar structure. Nat. Protoc. 7, 654.

Currey, J.D., 1988. The effect of porosity and mineral content on the Young's modulus of elasticity of compact bone. J Biomech 21, 131-139.
de Almeida Jackix, E., Cuneo, F., Amaya-Farfan, J., de Assuncao, J.V., Quintaes, K.D., 2010. A food supplement of hydrolyzed collagen improves compositional and biodynamic characteristics of vertebrae in ovariectomized rats. J Med Food 13, 1385-1390.
Diebold, J., Bätge, B., Stein, H., Müller-Esch, G., Müller, P.K., Löhrs, U., 1991. Osteoporosis in longstanding acromegaly: characteristic changes of vertebral trabecular architecture and bone matrix composition. Virchows Archiv. A, Pathological anatomy and histopathology 419, 209-215.
Donnelly, E., Chen, D.X., Boskey, A.L., Baker, S.P., van der Meulen, M.C.H., 2010. Contribution of mineral to bone structural behavior and tissue mechanical properties. Calcified tissue international 87, 450-460.
Ducourthial, G., Affagard, J.-S., Schmeltz, M., Solinas, X., Lopez-Poncelas, M., Bonod-Bidaud, C., Rubio-Amador, R., Ruggiero, F., Allain, J.-M., Beaurepaire, E., Schanne-Klein, M.-C., 2019. Monitoring dynamic collagen reorganization during skin stretching with fast polarization-resolved second harmonic generation imaging. Journal of biophotonics 12, e201800336.
Ehrnthaller, C., Huber-Lang, M., Nilsson, P., Bindl, R., Redeker, S., Recknagel, S., Rapp, A., Mollnes, T., Amling, M., Gebhard, F., Ignatius, A., 2013. Complement C3 and C5 deficiency affects fracture healing. PLoS One 8, e81341-e81341.
Florencio-Silva, R., Sasso, G.R.D., Sasso-Cerri, E., Simoes, M.J., Cerri, P.S., 2015. Biology of Bone Tissue: Structure, Function, and Factors That Influence Bone Cells. Biomed Res. Int., 17.
Forlino, A., Cabral, W.A., Barnes, A.M., Marini, J.C., 2011. New perspectives on osteogenesis imperfecta. Nat Rev Endocrinol 7, 540-557.
Fukushima, S.-i., Yonetsu, M., Yasui, T., 2018. Polarization-resolved second-harmonic-generation imaging of dermal collagen fiber in prewrinkled and wrinkled skins of ultraviolet-B-exposed mouse. Journal of biomedical optics 24, 031006.
Goldman, H.M., Bromage, T.G., Thomas, C.D., Clement, J.G., 2003. Preferred collagen fiber orientation in the human mid-shaft femur. Anat Rec A Discov Mol Cell Evol Biol 272, 434-445.
Goring, A., Sharma, A., Javaheri, B., Smith, R.C., Kanczler, J.M., Boyde, A., Hesse, E., Mahajan, S., Olsen, B.R., Pitsillides, A.A., Schneider, P., Oreffo, R.O., Clarkin, C.E., 2019. Regulation of the Bone Vascular Network is Sexually Dimorphic. J. Bone Miner. Res. 34, 2117-2132.
Haibo, Z., Guoping, C., Jingyuan, D., Zhidao, X., Lan, W., Tongbo, Z., 1997. Expression of matrix metalloproteinase-9 mRNA in osteoporotic bone tissues. Journal of Tongji Medical University 17, 28-31.
Houston, B., Stewart, A.J., Farquharson, C., 2004. PHOSPHO1—A novel phosphatase specifically expressed at sites of mineralisation in bone and cartilage. Bone 34, 629-637.
Hu, K., Olsen, B.R., 2016. Osteoblast-derived VEGF regulates osteoblast differentiation and bone formation during bone repair. The Journal of clinical investigation 126, 509-526.
James, D., Jambor, A., Chang, H.-Y., Alden, Z., Tilbury, K., Sandbo, N., Campagnola, P., 2019. Probing ECM remodeling in idiopathic pulmonary fibrosis via second harmonic generation microscopy analysis of macro/supramolecular collagen structure. Journal of biomedical optics 25, 014505.
Javaheri, B., Carriero, A., Staines, K.A., Chang, Y.M., Houston, D.A., Oldknow, K.J., Millan, J.L., Kazeruni, B.N., Salmon, P., Shefelbine, S., Farquharson, C., Pitsillides, A.A., 2015. Phospho1 deficiency transiently modifies bone architecture yet produces consistent modification in osteocyte differentiation and vascular porosity with ageing. Bone 81, 277-291.
Johnson, P., Karvounis, A., Singh, H.J., Brereton, C.J., Bourdakos, K., Lunn, K., Roberts, J.J., Davies, D.E., Muskens, O.L., Jones, M.G., Mahajan, S., 2020. Super-resolved polarisation-enhanced second harmonic generation for direct imaging of nanoscale changes in collagen architecture. bioRxiv, 2020.2002.2007.934000.
Kafantari, H., Kounadi, E., Fatouros, M., Milonakis, M., Tzaphlidou, M., 2000. Structural alterations in rat skin and bone collagen fibrils induced by ovariectomy. Bone 26, 349-353.

Keeting, P.E., Scott, R.E., Colvard, D.S., Han, I.K., Spelsberg, T.C., Riggs, B.L., 1991. Lack of a direct effect of estrogen on proliferation and differentiation of normal human osteoblast-like cells. Journal of bone and mineral research : the official journal of the American Society for Bone and Mineral Research 6, 297-304.
König, D., Oesser, S., Scharla, S., Zdzieblik, D., Gollhofer, A., 2018. Specific Collagen Peptides Improve Bone Mineral Density and Bone Markers in Postmenopausal Women-A Randomized Controlled Study. Nutrients 10, 97.
Le Goff, C., Somerville, R.P.T., Kesteloot, F., Powell, K., Birk, D.E., Colige, A.C., Apte, S.S., 2006. Regulation of procollagen amino-propeptide processing during mouse embryogenesis by specialization of homologous ADAMTS proteases: insights on collagen biosynthesis and dermatosparaxis. Development (Cambridge, England) 133, 1587-1596.
Li, S., Demirci, E., Silberschmidt, V.V., 2013. Variability and anisotropy of mechanical behavior of cortical bone in tension and compression. Journal of the Mechanical Behavior of Biomedical Materials 21, 109-120.
Lin, J., Pan, S., Zheng, W., Huang, Z., 2013. Polarization-resolved second-harmonic generation imaging for liver fibrosis assessment without labeling. Applied Physics Letters 103, 173701.
Liu, Y., Berendsen, A.D., Jia, S., Lotinun, S., Baron, R., Ferrara, N., Olsen, B.R., 2012. Intracellular VEGF regulates the balance between osteoblast and adipocyte differentiation. The Journal of clinical investigation 122, 3101-3113.
Livak, K.J., Schmittgen, T.D., 2001. Analysis of Relative Gene Expression Data Using Real-Time Quantitative PCR and the 2−ΔΔCT Method. Methods 25, 402-408.
Madupalli, H., Pavan, B., Tecklenburg, M.M.J., 2017. Carbonate substitution in the mineral component of bone: Discriminating the structural changes, simultaneously imposed by carbonate in A and B sites of apatite. Journal of solid state chemistry 255, 27-35.
Majeska, R.J., Ryaby, J.T., Einhorn, T.A., 1994. Direct modulation of osteoblastic activity with estrogen. The Journal of bone and joint surgery. American volume 76, 713-721.
Mandair, G.S., Morris, M.D., 2015. Contributions of Raman spectroscopy to the understanding of bone strength. BoneKEy Rep. 4, 8.
Mansfield, J.C., Mandalia, V., Toms, A., Winlove, C.P., Brasselet, S., 2019. Collagen reorganization in cartilage under strain probed by polarization sensitive second harmonic generation microscopy. J. R. Soc. Interface 16, 20180611.
Markova, M.S., Zeskand, J., McEntee, B., Rothstein, J., Jimenez, S.A., Siracusa, L.D., 2004. A Role for the Androgen Receptor in Collagen Content of the Skin. Journal of Investigative Dermatology 123, 1052-1056.
Martin, R.B., Boardman, D.L., 1993. The effects of collagen fiber orientation, porosity, density, and mineralization on bovine cortical bone bending properties. Journal of Biomechanics 26, 1047-1054.
McCreadie, B.R., Morris, M.D., Chen, T.-c., Sudhaker Rao, D., Finney, W.F., Widjaja, E., Goldstein, S.A., 2006. Bone tissue compositional differences in women with and without osteoporotic fracture. Bone 39, 1190-1195.
McElderry, J.-D.P., Zhu, P., Mroue, K.H., Xu, J., Pavan, B., Fang, M., Zhao, G., McNerny, E., Kohn, D.H., Franceschi, R.T., Holl, M.M.B., Tecklenburg, M.M.J., Ramamoorthy, A., Morris, M.D., 2013. Crystallinity and compositional changes in carbonated apatites: Evidence from (31)P solid-state NMR, Raman, and AFM analysis. Journal of solid state chemistry 206, 10.1016/j.jssc.2013.1008.1011.
Morgan, E.F., Unnikrisnan, G.U., Hussein, A.I., 2018. Bone Mechanical Properties in Healthy and Diseased States. Annu Rev Biomed Eng 20, 119-143.
Morris, M.D., Mandair, G.S., 2011. Raman assessment of bone quality. Clinical orthopaedics and related research 469, 2160-2169.
Mostaço-Guidolin, L., Rosin, N.L., Hackett, T.-L., 2017. Imaging Collagen in Scar Tissue: Developments in Second Harmonic Generation Microscopy for Biomedical Applications. Int. J. Mol. Sci. 18, 1772.

Nadiarnykh, O., Plotnikov, S., Mohler, W.A., Kalajzic, I., Redford-Badwal, D., Campagnola, P.J., 2007. Second harmonic generation imaging microscopy studies of osteogenesis imperfecta. Journal of biomedical optics 12, 051805.
Nair, A.K., Gautieri, A., Chang, S.-W., Buehler, M.J., 2013. Molecular mechanics of mineralized collagen fibrils in bone. Nature communications 4, 1724.
Nunez, J.A., Goring, A., Javaheri, B., Razi, H., Gomez-Nicola, D., Pitsillides, A.A., Thurner, P.J., Gomez-Nicola, D., Schneider, P., Clarkin, C.E., 2018. Regional diversity in the murine cortical vascular network is revealed by synchrotron X-ray tomography and is amplified with age. European cells & materials 35, 281-299.
Nyman, J.S., Makowski, A.J., 2012. The Contribution of the Extracellular Matrix to the Fracture Resistance of Bone. Current osteoporosis reports 10, 169-177.
Olejnik, C., Falgayrac, G., During, A., Cortet, B., Penel, G., 2016. Doses effects of zoledronic acid on mineral apatite and collagen quality of newly-formed bone in the rat's calvaria defect. Bone 89, 32-39.
Orriss, I.R., Hajjawi, M.O., Huesa, C., MacRae, V.E., Arnett, T.R., 2014. Optimisation of the differing conditions required for bone formation in vitro by primary osteoblasts from mice and rats. Int J Mol Med 34, 1201-1208.
Park, J., Fertala, A., Tomlinson, R.E., 2019. Naproxen impairs load-induced bone formation, reduces bone toughness, and diminishes woven bone formation following stress fracture in mice. Bone 124, 22-32.
Pinsard, M., Laverty, S., Richard, H., Dubuc, J., Schanne-Klein, M.-C., Légaré, F., 2019. Maturation of the Meniscal Collagen Structure Revealed by Polarization-Resolved and Directional Second Harmonic Generation Microscopy. Sci Rep 9, 18448.
Pleshko, N., Boskey, A., Mendelsohn, R., 1991. Novel infrared spectroscopic method for the determination of crystallinity of hydroxyapatite minerals. Biophysical Journal 60, 786-793.
Pologruto, T.A., Sabatini, B.L., Svoboda, K., 2003. ScanImage: flexible software for operating laser scanning microscopes. Biomed Eng Online 2, 13.
Ramshaw, J.A., Shah, N.K., Brodsky, B., 1998. Gly-X-Y tripeptide frequencies in collagen: a context for host-guest triple-helical peptides. J Struct Biol 122, 86-91.
Riikonen, T., Westermarck, J., Koivisto, L., Broberg, A., Kähäri, V.M., Heino, J., 1995. Integrin alpha 2 beta 1 is a positive regulator of collagenase (MMP-1) and collagen alpha 1(I) gene expression. J Biol Chem 270, 13548-13552.
Rouède, D., Schaub, E., Bellanger, J.-J., Ezan, F., Scimeca, J.-C., Baffet, G., Tiaho, F., 2017. Determination of extracellular matrix collagen fibril architectures and pathological remodeling by polarization dependent second harmonic microscopy. Sci Rep 7, 12197.
Schindelin, J., Arganda-Carreras, I., Frise, E., Kaynig, V., Longair, M., Pietzsch, T., Preibisch, S., Rueden, C., Saalfeld, S., Schmid, B., Tinevez, J.Y., White, D.J., Hartenstein, V., Eliceiri, K., Tomancak, P., Cardona, A., 2012. Fiji: an open-source platform for biological-image analysis. Nat Methods 9, 676-682.
Scott, A.D., Martin, F.L., Trevisan, J., Carmichael, P.L., Angelov, P.P., 2013. IRootLab: a free and open-source MATLAB toolbox for vibrational biospectroscopy data analysis. Bioinformatics 29, 1095-1097.
Seeman, E., 2001. Sexual Dimorphism in Skeletal Size, Density, and Strength. The Journal of Clinical Endocrinology & Metabolism 86, 4576-4584.
Senel, K., Baykal, T., Seferoglu, B., Altas, E.U., Baygutalp, F., Ugur, M., Kiziltunc, A., 2013. Circulating vascular endothelial growth factor concentrations in patients with postmenopausal osteoporosis. Archives of medical science : AMS 9, 709-712.
Sharma, A., Goring, A., Staines, K.A., Emery, R.J.H., Pitsillides, A.A., Oreffo, R.O.C., Mahajan, S., Clarkin, C.E., 2020. Raman spectroscopy links differentiating osteoblast matrix signatures to pro-angiogenic potential. Matrix Biology Plus 5, 100018.
Shoulders, M.D., Raines, R.T., 2009. Collagen structure and stability. Annual review of biochemistry 78, 929-958.

Simkin, A., Robin, G., 1974. Fracture formation in differing collagen fiber pattern of compact bone. Journal of Biomechanics 7, 183-188.
Smith, S.J., Emery, R., Pitsillides, A., Clarkin, C.E., Mahajan, S., 2017. Detection of early osteogenic commitment in primary cells using Raman spectroscopy. Analyst 142, 1962-1973.
Son, E.D., Lee, J.Y., Lee, S., Kim, M.S., Lee, B.G., Chang, I.S., Chung, J.H., 2005. Topical Application of 17β-Estradiol Increases Extracellular Matrix Protein Synthesis by Stimulating TGF-β Signaling in Aged Human Skin In Vivo. Journal of Investigative Dermatology 124, 1149-1161.
Sroga, G.E., Vashishth, D., 2012. Effects of bone matrix proteins on fracture and fragility in osteoporosis. Current osteoporosis reports 10, 141-150.
Staines, K.A., MacRae, V.E., Farquharson, C., 2012. The importance of the SIBLING family of proteins on skeletal mineralisation and bone remodelling. The Journal of endocrinology 214, 241-255.
Stoller, P., Reiser, K.M., Celliers, P.M., Rubenchik, A.M., 2002. Polarization-modulated second harmonic generation in collagen. Biophys J 82, 3330-3342.
Su, P.-J., Chen, W.-L., Hong, J.-B., Li, T.-H., Wu, R., Jr., Chou, C.-K., Chen, S.-J., Hu, C., Lin, S.-J., Dong, C.-Y., 2009. Discrimination of collagen in normal and pathological skin dermis through second-order susceptibility microscopy. Opt. Express 17, 11161-11171.
Suarez, K.N., Romanello, M., Bettica, P., Moro, L., 1996. Collagen type I of rat cortical and trabecular bone differs in the extent of posttranslational modifications. Calcif Tissue Int 58, 65-69.
Thevenaz, P., Unser, M., 2007. User-friendly semiautomated assembly of accurate image mosaics in microscopy. Microscopy research and technique 70, 135-146.
Tilbury, K., Hocker, J., Wen, B.L., Sandbo, N., Singh, V., Campagnola, P.J., 2014a. Second harmonic generation microscopy analysis of extracellular matrix changes in human idiopathic pulmonary fibrosis. Journal of biomedical optics 19, 086014-086014.
Tilbury, K., Lien, C.-H., Chen, S.-J., Campagnola, Paul J., 2014b. Differentiation of Col I and Col III Isoforms in Stromal Models of Ovarian Cancer by Analysis of Second Harmonic Generation Polarization and Emission Directionality. Biophysical Journal 106, 354-365.
Tokarz, D., Cisek, R., Joseph, A., Golaraei, A., Mirsanaye, K., Krouglov, S., Asa, S.L., Wilson, B.C., Barzda, V., 2019. Characterization of Pancreatic Cancer Tissue Using Multiphoton Excitation Fluorescence and Polarization-Sensitive Harmonic Generation Microscopy. Frontiers in Oncology 9.
Unal, M., Creecy, A., Nyman, J.S., 2018. The Role of Matrix Composition in the Mechanical Behavior of Bone. Current osteoporosis reports 16, 205-215.
Van Gulick, L., Saby, C., Morjani, H., Beljebbar, A., 2019. Age-related changes in molecular organization of type I collagen in tendon as probed by polarized SHG and Raman microspectroscopy. Sci Rep 9, 7280.
Vandenabeele, P., 2013. *Practical Raman spectroscopy: an introduction*. Wiley & Sons, Chichester, UK.
Viguet-Carrin, S., Garnero, P., Delmas, P.D., 2006. The role of collagen in bone strength. Osteoporosis international : a journal established as result of cooperation between the European Foundation for Osteoporosis and the National Osteoporosis Foundation of the USA 17, 319-336.
Wang, Y., Azaïs, T., Robin, M., Vallée, A., Catania, C., Legriel, P., Pehau-Arnaudet, G., Babonneau, F., Giraud-Guille, M.-M., Nassif, N., 2012. The predominant role of collagen in the nucleation, growth, structure and orientation of bone apatite. Nat. Mater. 11, 724-733.
Watanabe-Kamiyama, M., Shimizu, M., Kamiyama, S., Taguchi, Y., Sone, H., Morimatsu, F., Shirakawa, H., Furukawa, Y., Komai, M., 2010. Absorption and effectiveness of orally administered low molecular weight collagen hydrolysate in rats. J Agric Food Chem 58, 835-841.
Wiren, K.M., Semirale, A.A., Zhang, X.-W., Woo, A., Tommasini, S.M., Price, C., Schaffler, M.B., Jepsen, K.J., 2008. Targeting of androgen receptor in bone reveals a lack of androgen anabolic action and inhibition of osteogenesis: a model for compartment-specific androgen action in the skeleton. Bone 43, 440-451.

Yao, X., Carleton, S.M., Kettle, A.D., Melander, J., Phillips, C.L., Wang, Y., 2013. Gender-dependence of bone structure and properties in adult osteogenesis imperfecta murine model. Ann Biomed Eng 41, 1139-1149.
Yerramshetty, J.S., Akkus, O., 2008. The associations between mineral crystallinity and the mechanical properties of human cortical bone. Bone 42, 476-482.
Zhou, S.-H., Yang, W.-J., Liu, S.-W., Li, J., Zhang, C.-Y., Zhu, Y., Zhang, C.-P., 2014. Gene expression profiling of craniofacial fibrous dysplasia reveals ADAMTS2 overexpression as a potential marker. Int J Clin Exp Pathol 7, 8532-8541.

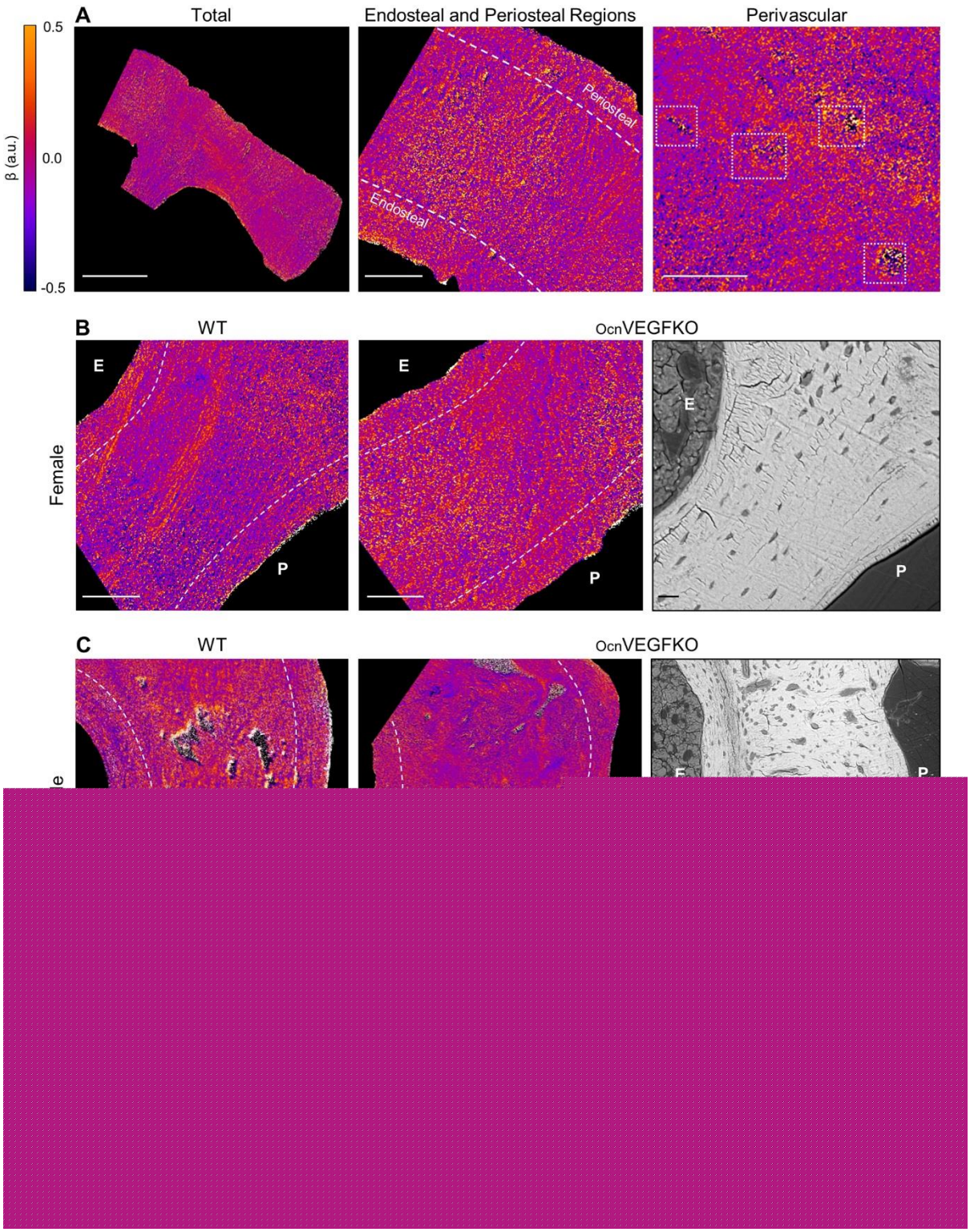

Fig. 3. SHG polarisation anisotropy identifies morphological disorder in collagen fibril alignment in the posterior region of the TFJ following OcnVEGFKO. Polarisation-resolved anisotropy analysis was performed on the total posterior region (A; left) on the endosteal and periosteal areas (middle; hatched lines) and around the vascular canals (right; boxed). Zoomed SHG polarisation anisotropy images of the posterior region of the TFJ are shown for female WT (B; left), female OcnVEGFKO (B; middle), male WT (C; left) and male OcnVEGFKO (C; middle) around the endosteal (depicted E) and periosteal (depicted P) regions. BSE-SEM images show endosteal and periosteal differences following

OcnVEGFKO in females (B; right) and males (C; right). The anisotropy parameter, β, calculated pixel-wise across the whole posterior region (D), around the endosteal (E) and periosteal regions (F), and around blood vessel canals (G) highlighted sex differences in local fibril organisation in WTs and OcnVEGFKOs animals and following VEGF depletion in OcnVEGFKOs versus WT controls. Data presented as mean anisotropy value ± SEM from n=3 female and n=3 male bone sections per genotype. Statistical significance between groups was assessed using Student's t-test (* $P<0.05$, ** $P<0.01$). Interaction between sex and genotype was assessed using Two-Way ANOVA. Scale bars in total anisotropy images represent 200 µm (A; left), with those in zoomed anisotropy images representing 50 µm. Scale bars in the BSE-SEM image correspond 100 µm (B) and 10 µm (C).

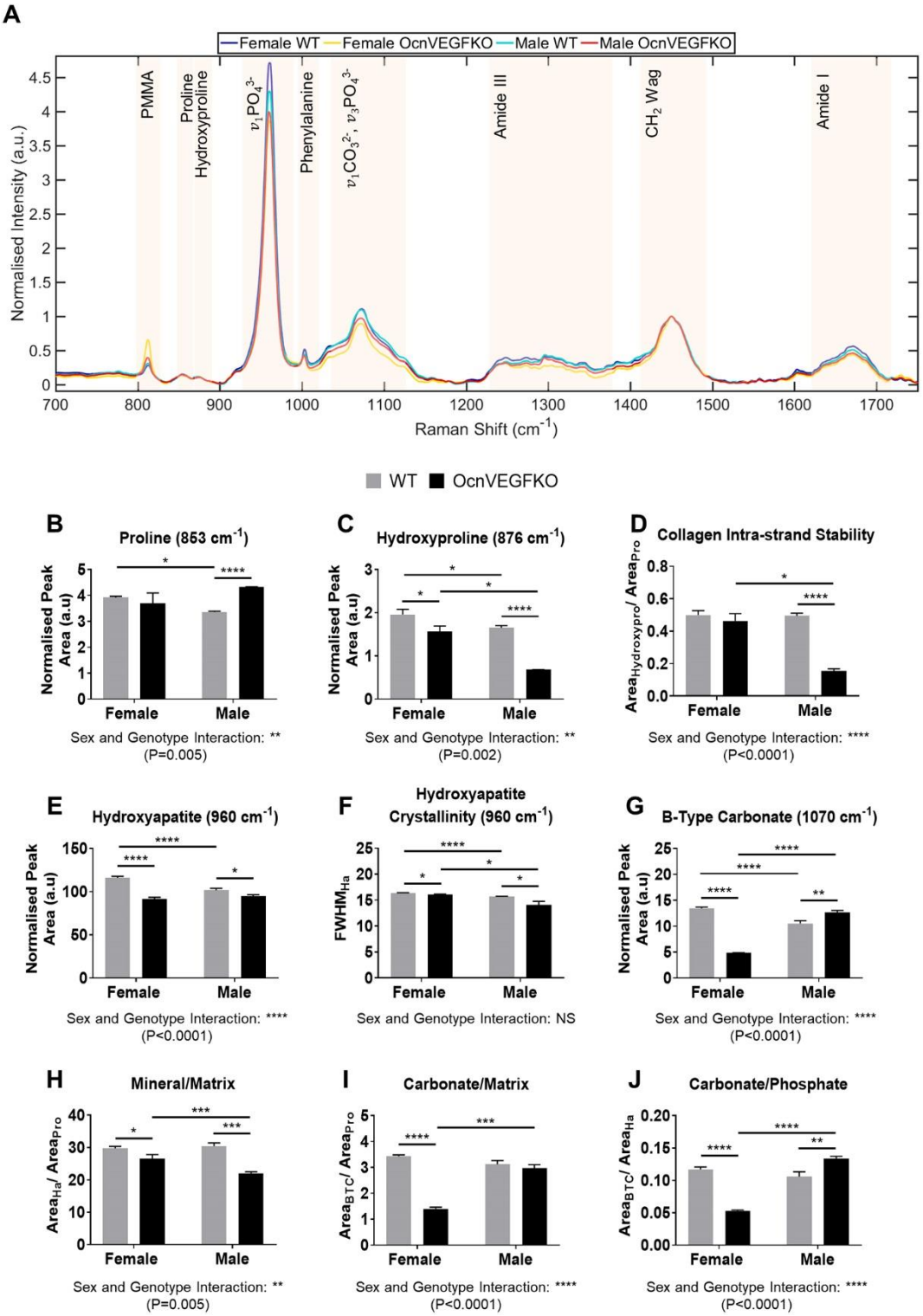

Fig. 4. Raman spectroscopy identifies correlative sexual dimorphism in bone matrix signatures. Deviations in class means of normalised spectra (n=75 spectra per group) were observed in Raman bands associated with the organic bone ECM (proline; 853 cm^{-1} and hydroxyproline; 876 cm^{-1}, amide III region; 1242 cm^{-1}, CH_2 deformation; 1450 cm^{-1} and amide I; 1660 cm^{-1}) and mineral components (hydroxyapatite, $v_1PO_4^{3-}$; 960 cm^{-1} and B-type carbonate; 1070 cm^{-1}) across the sexes between genotypes (A). Spectral deconvolution of Raman spectra revealed sex differences in components associated with mature type I collagen (proline; B and hydroxyproline; C) in WT and OcnVEGFKO

animals, in addition to sex-specific VEGF effects in following OcnVEGFKO versus WTs. These changes resulted in a reduction in the collagen intra-strand stability (D), with sex differences detected in OcnVEGFKO animals, and in male OcnVEGFKO bones versus WT controls. Diversity in the levels of hydroxyapatite (HA; E), HA crystallinity (F) and B-type carbonate (G) were also detected across the sexes and genotypes. The dimorphic modifications to the collagen-specific and mineral species, emphasised by the mineral/matrix ratio (H), the carbonate/matrix ratio (I) and the carbonate/phosphate ratio (J), highlighted additional sex differences between WT and OcnVEGFKO animals and the sex-specific effects of VEGF loss between OcnVEGFKO and WT controls. Data presented as the mean normalised peak area or full-width half-maximum (FWHM) ± SEM from n=3 female and n=3 male bone sections per genotype. Statistical significance between groups was assessed using Student's t-test (* $P<0.05$, ** $P<0.01$, *** $P<0.001$, **** $P<0.0001$). Interaction between sex and genotype was assessed using Two-Way ANOVA.

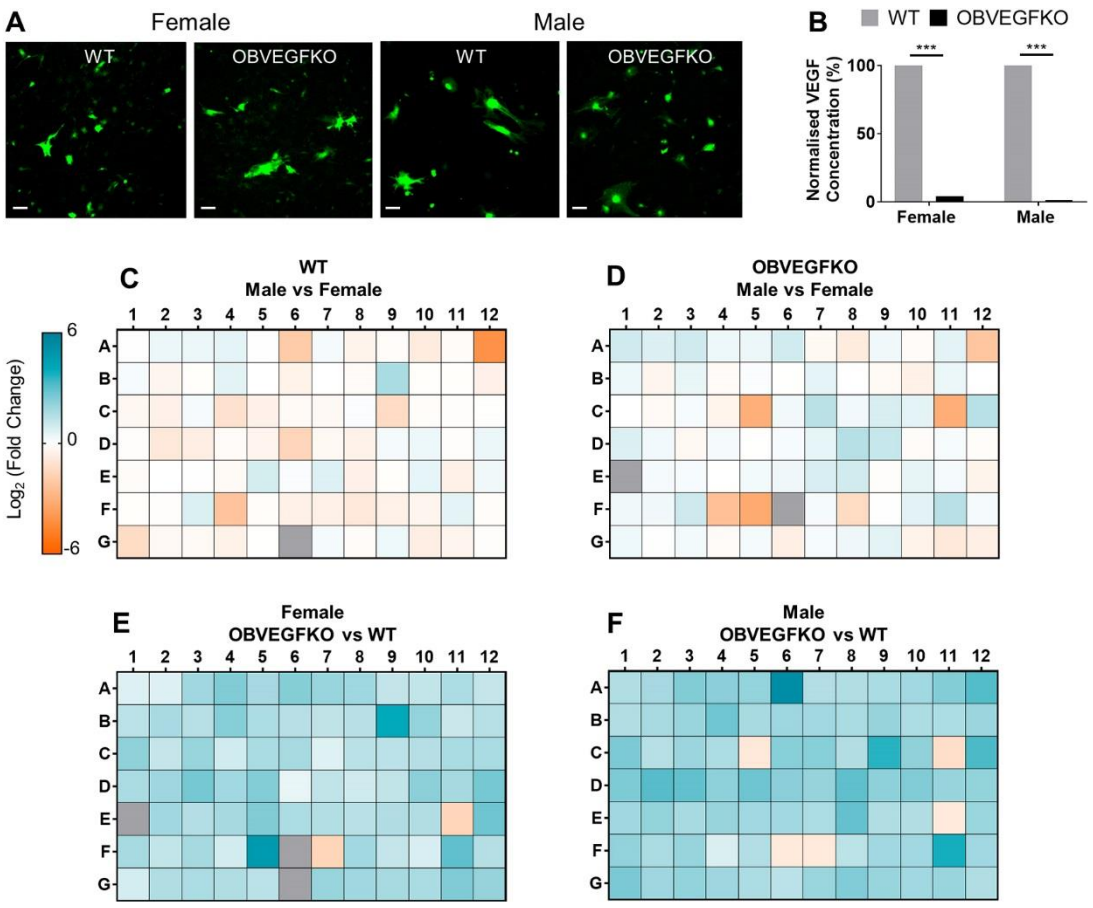

G

	Gene	WT Male vs Female (Fold Change)	OBVEGFKO Male vs Female (Fold Change)	Female OBVEGFKO vs WT (Fold Change)	Male OBVEGFKO vs WT (Fold Change)
Matrix Formation and Mineralisation	*Col1a1*	-1.14	1.48	3.17	5.33
	Itga2	-1.21	2.62	1.56	4.92
	Itgae	-1.1	-8.96	3.28	-2.48
	Spp1	-1.11	1.15	2.8	3.59
Matrix Remodelling	*Adamts2*	-1.31	1.63	1.6	3.44
	Hc	-1.44	-8.72	3.18	-1.9
	Mmp13	1.83	1.19	5.51	3.59
	Sparc	-1.33	1.54	1.74	3.57
Angiogenesis	*Lama1*	-1.46	2.76	1.96	7.89
	Mmp9	-1.07	1.24	3.37	4.44
	Thbs1	-1.19	1.2	3.09	4.39

Fig. 5. Deletion of VEGF in osteoblasts *in vitro* drives alterations in gene expression associated with extracellular matrix organisation and composition. Representative fluorescence images of primary murine male and female OBs transduced with adenovirus expressing GFP (WT) or expressing Cre-recombinase (OBVEGFKO) *in vitro* are shown (A). Knockdown was confirmed by VEGF-A ELISA of conditioned media (B). mRNA expression of 84 genes associated with the ECM and adhesion molecules, screened by qPCR array (n=1 cDNA), are displayed as heatmap diagrams of log transformed fold change in relative expression levels. Heatmaps highlight sex differences between WT cells (C) and OBVEGFKO cells (D) in addition to the effect of OBVEGFKO in female (E) and male (F) OBs versus *Vegf*-expressing WTs. Table summarising effect of OBVEGFKO on the expression of key genes expressed as fold change (G). Scale bars represent 100 μm.

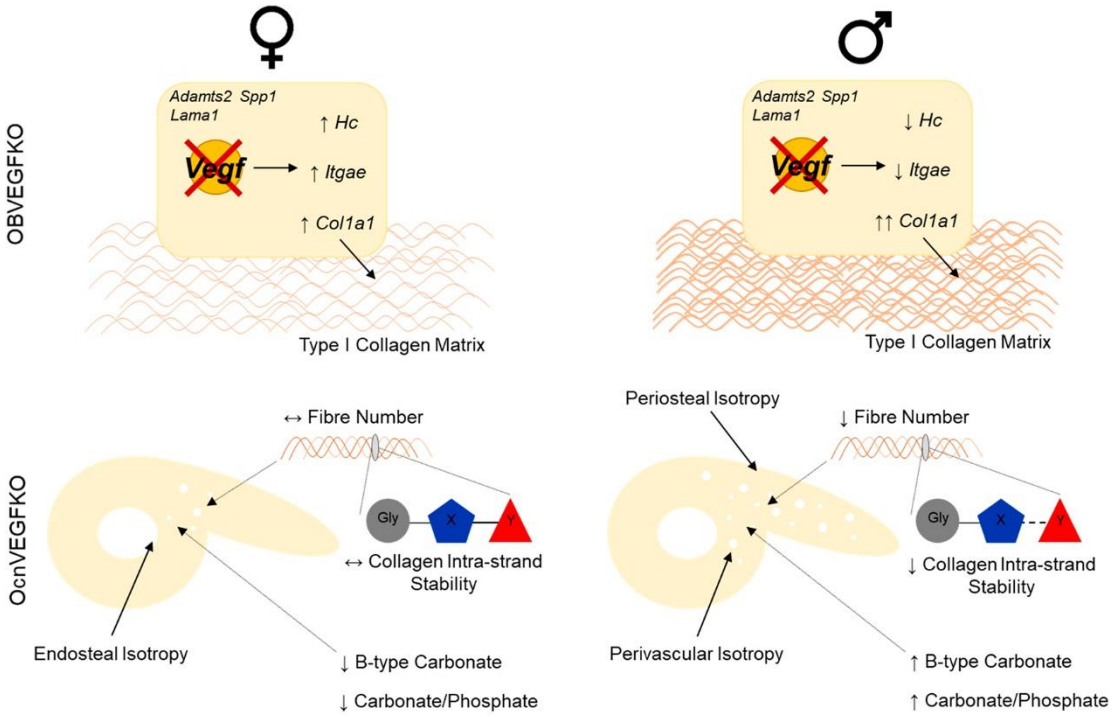

Fig. 6. Multiscale sexual dimorphism of the bone matrix is induced following the deletion of VEGF. In female OcnVEGFKO bones, localised deformation of collagen fibril arrangement was confined to the endosteal region of the posterior cortex at the TFJ, with no detectable change to collagen fibre number. Collagen intra-strand stability was unaffected however reduction in the levels of B-type carbonate were coupled to further sex-specific reductions in the carbonate/phosphate ratio following OcnVEGFKO. In contrast, the loss of VEGF in male OcnVEGFKOs resulted in modified arrangement of collagen fibrils around the posterior periosteal region and perivascular canals, paired with reduction in fibre number and loss of intra-strand stability. These effects were associated with increases in both B-type carbonate and the carbonate/phosphate ratio. These macroscale changes in organisation and nanoscale alterations in composition could be indicative of a direct role of VEGF in the sex-specific regulation of ECM formation and remodelling *in vitro*, identified following the deletion of OB-derived VEGF in male and female cell cultures.

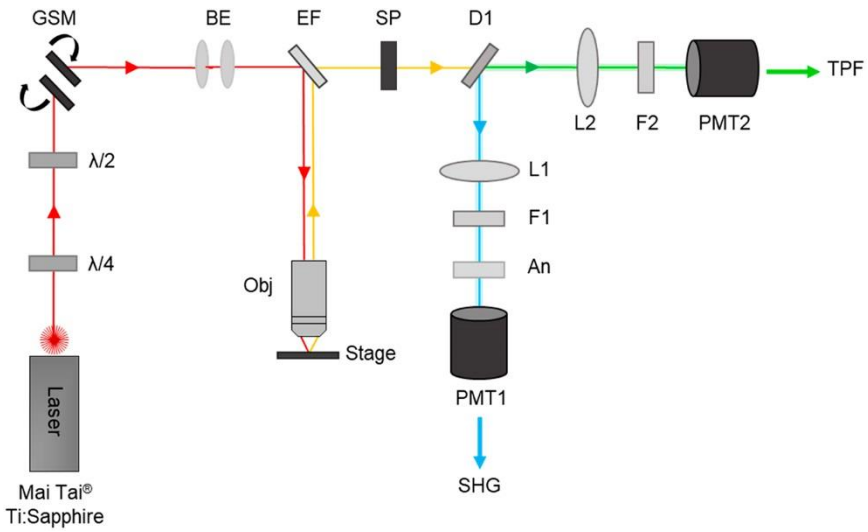

Fig. 7. Schematic of the multiphoton laser scanning system. The femtosecond pulsed Titanium: Sapphire laser, tuned to produce an output at 808 nm (red), passes through a quarter (λ/4) and half (λ/2) waveplate allowing control of the polarisation state of the fundamental beam. The beam is directed towards a pair of galvanometric mirrors (GSM) to enable laser scanning, followed by a beam expander (BE) prior to being directed to the stage-mounted sample through an excitation filter (EF) and microscope objective (Obj). The generated sample-signal (yellow) is backwards collected through the objective and separated from the excitation wavelength by the same EF and short pass (SP) filter. SHG signal (blue) is isolated from TPEF by a dichroic beam splitter (D1) and directed onto a photomultiplier tube (PMT1) after being focused (L1) and filtered (F1). A linear analyser (An), placed ahead of PMT1 after F1 enables detection of polarisation-dependent SHG emissions. TPEF signals (green) are similarly focused (L2) and filtered (F2) before detection by PMT2.

Supplementary Information

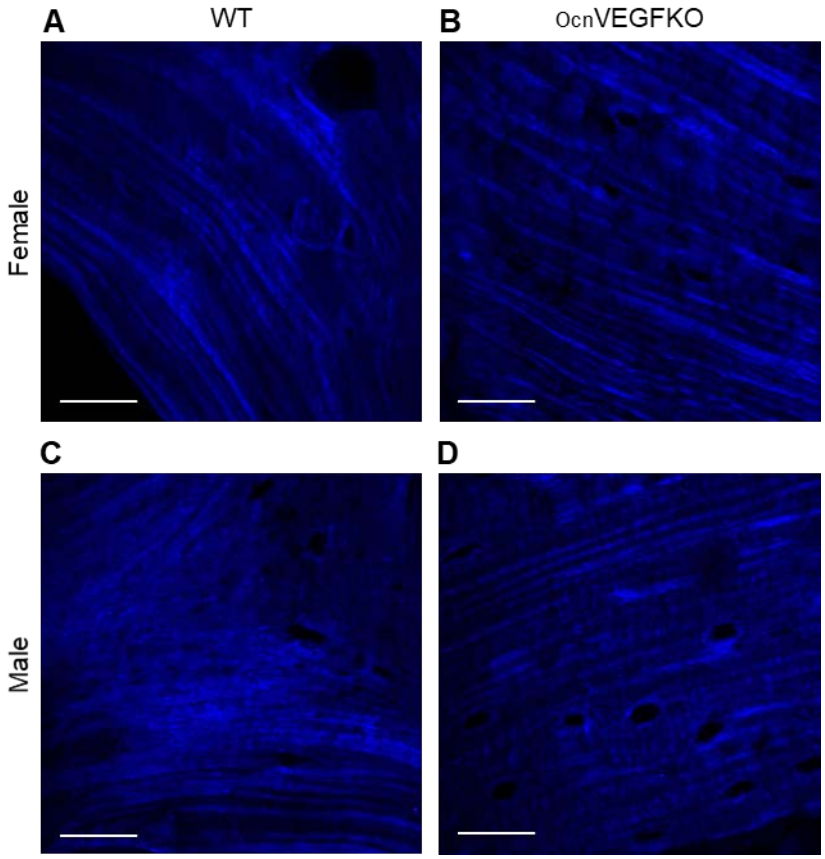

Fig. S1. High magnification p-SHG images of PMMA embedded sections reveal collagen fibres in female WT (A), female OcnVEGFKO (B), male WT (C) and male OcnVEGFKO (D) sections. Scale bars represent 50 µm.

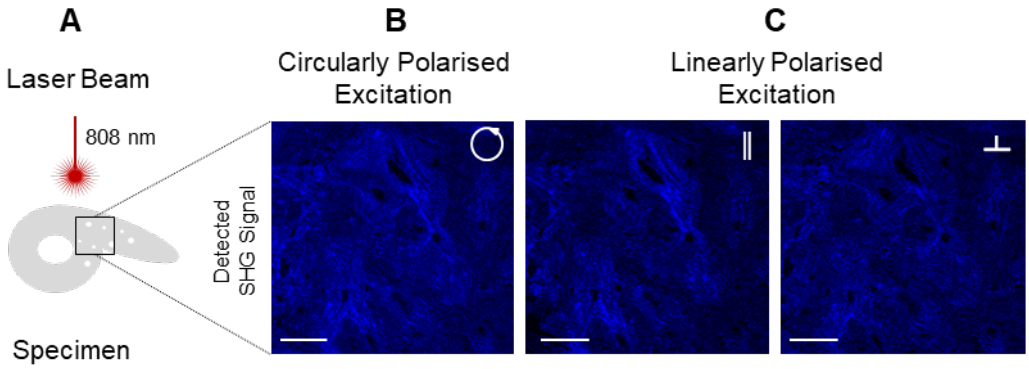

Fig. S2. Visualisation of bone matrix collagen fibres is polarisation dependent. SHG images of PMMA embedded sections were acquired by tuning the wavelength of the fundamental excitation laser to 808 nm (A). Circular polarisation of the fundamental beam, achieved by modulation of λ/4 and λ/2 waveplates, enabled uniform excitation of collagen fibrils (B) orientated in all directions across the specimen. Linear polarisation enables excitation of collagen fibrils that are orientated parallel (C; ∥, left) or orthogonal (C; ⊥, right) to polarisation of the fundamental laser, showing maximum intensity with alignment at 0 ° (∥) and minimum at 90 ° (⊥). Scale bars represent 50 µm.

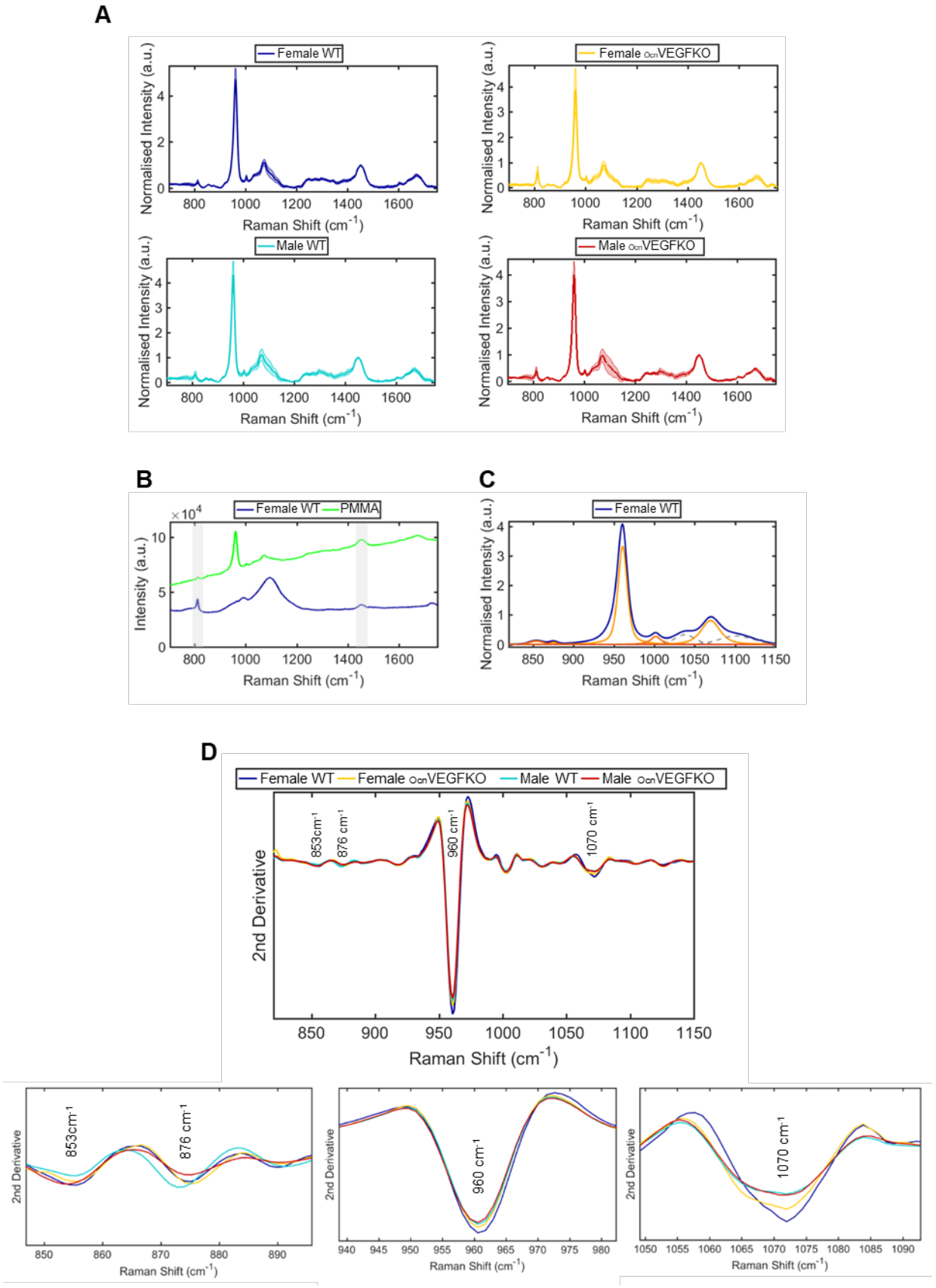

Fig. S3. Raman spectra collected within the fingerprint region from 700 cm^{-1} to 1750 cm^{-1} from the posterior region of three littermate matched female WT, female OcnVEGFKO, male WT and male OcnVEGFKO TFJ sections are presented as class means of n=75 single spectra with SD displayed (A).

PMMA contributions in bone Raman spectra are highlighted in raw, unprocessed spectra ahead of deconvolution analysis. Peaks of interest associated with the ECM (proline, 853 cm^{-1} and hydroxyproline, 876 cm^{-1} in type I collagen) and mineral (HA, 960 cm^{-1} and B-type carbonate, 1070 cm^{-1}), displayed as orange lines (C) are identifiable in bone Raman spectra following the calculation of second derivative spectra (D). Zoomed spectral peaks of interest identified in the second derivative spectra shown underneath (D) were analysed further by spectral deconvolution.